

# Chapter 3

## Apparatus

### 3.1 Overview

This chapter will describe the production and delivery of muons, the time expansion chambers that measured the muon beam, and the detector used to track the muons and reconstruct the positron trajectories. The alignment and calibration of the apparatus will also be described. There are publications that provide more detail on the detector[29] and time expansion chambers[30]. The beam line has been described in an earlier publication[31], but the tune used for the current experiment is only available as an internal report[32].

### 3.2 Muon production and delivery

#### 3.2.1 Location

The experiment took place at the TRIUMF laboratory, located on the University of British Columbia's campus. The TRIUMF cyclotron delivered a 500 MeV proton beam to the T1 production target in the TRIUMF meson hall. The protons were delivered in bunches of 4 ns width, with each bunch separated by 43 ns. For the data in this thesis, a graphite production target was used at the T1 position. In previous data acquisition, a beryllium target was used, but this resulted in an undesirable beam spot and high positron contamination. The particles from the graphite target were selected by a secondary beam line named M13. The experiment occupied the M13 beam line area from November 2001 to September 2007.

#### 3.2.2 Muon production

The proton beam incident on the graphite target produced pions. The dominant pion decay is to a muon and neutrino, a two body process that ensures the muon has momentum  $29.79 \text{ MeV}/c$  in the pion centre of mass frame. The experiment selected positive muons<sup>8</sup> that

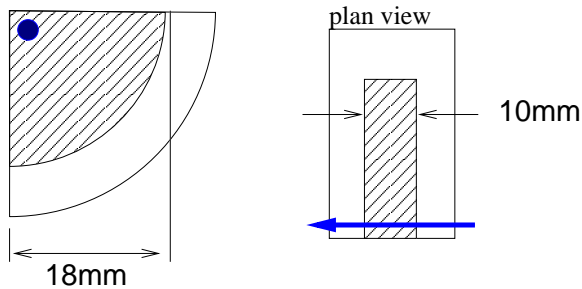
---

<sup>8</sup>A negative muon beam can be selected from negative pion decays in the production target by reversing the polarity of the beam line steering elements. However, the negative muon rate is considerably lower because the muons interact with the production target nuclei and are captured into atomic orbits. One week of

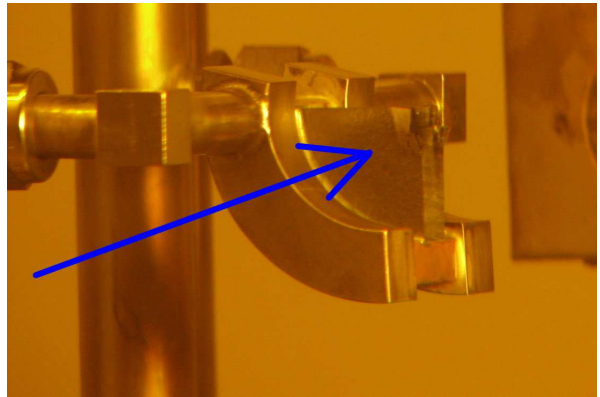
decayed from stationary pions at the surface of the production target. These are known as “surface muons” and are highly polarised as described in Section 2.0.3.

The graphite production target is shown schematically in Fig. 3.1(a), and was located in a water cooled steel holder. The targets typically lasted longer than a month, and were changed either due to destructive damage from the proton beam (see Fig. 3.1(b)) or after producing measurable levels of radioactive gas. The gas did not impair the data quality since it was mostly stopped by a  $3\ \mu\text{m}$  polyester window valve in the beam line, and any particles making it to detector were successfully identified using the experiment’s event reconstruction software. In addition, for the data acquired in 2007, a pump was installed in M13 to remove any radioactive gas making it past the window valve.

10mm Graphite



(a) Schematic of the graphite production target. The blue arrow indicates the proton beam.



(b) Photograph of a damaged graphite production target. The blue arrow indicates the proton beam direction.

Figure 3.1: Schematic and photograph of a graphite production target.

### 3.2.3 M13 beam line

The M13 beam line that selects and transports the muons is shown schematically in Fig. 3.2, with the graphite production target labelled as 1AT1, which is seen by M13 at  $135^\circ$ . The channel has two dipole magnets at  $60^\circ$  to the beam (B1 and B2) that select the particle momentum, three vertically focusing quadrupole magnets (Q1, Q4, Q7) and four horizontally focusing quadrupoles magnets (Q3, Q5, Q6). The M13 beam line was upgraded for the current

---

negative muon data was accumulated using an aluminium stopping target and this data is undergoing an independent analysis.

measurement by adding current sources to certain quadrupole magnets, allowing additional muon beam steering; this technique will be described in Section 3.4.

Figure 3.2 indicates a horizontal slit and vertical jaw upstream of B1. These control both the rate and angular spread of the beam. A compromise must be reached that minimises emittance while maintaining an acceptance rate. Muon rates between 2 kHz and 5 kHz were used for the data in this thesis. Even at the highest rate the muons are separated by nearly 100 lifetimes, ensuring most events have just one muon in the detector at a time.

The figure also indicates three possible focal points (F1, F2 and F3). In the tune used for the current experiment there is a horizontal and vertical focus<sup>9</sup> at F2 but at F1 there is only a horizontal focus, *not* a vertical focus. This results in a vertically larger beam at the jaws and hence more precise selection of initial vertical divergence[32][33]. After B1 has dispersed the beam, the position of the horizontal slit at F1 selects the momentum, and the width of this slit selects the momentum resolution of the channel.

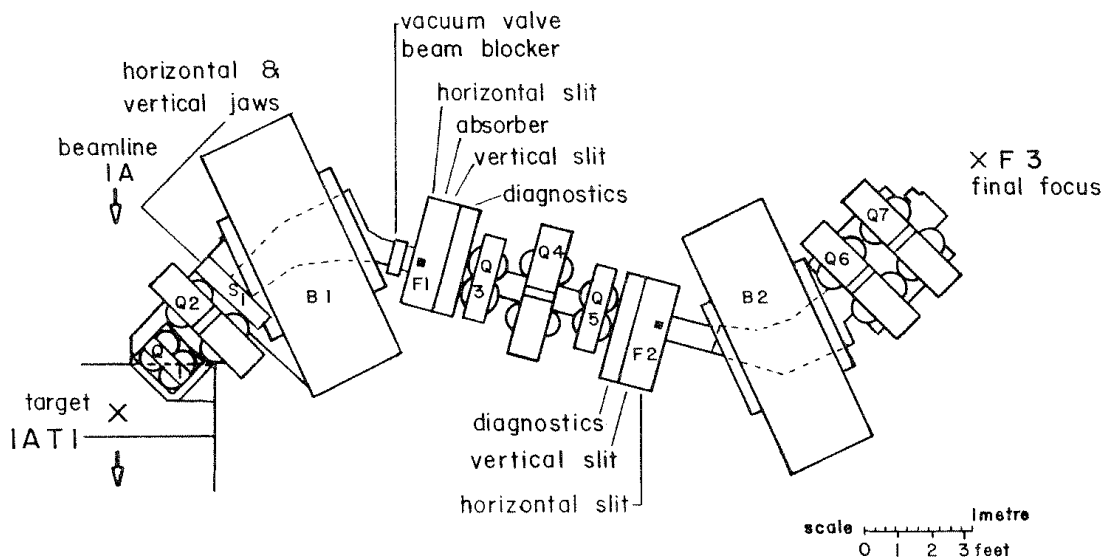


Figure 3.2: Schematic of the M13 beam line[31]. The distance from the production target to the centre of the detector (not shown) is approximately 10m.

<sup>9</sup>A beam line focus is analogous to an optical focus, where the beamspot size is very small, but the angle of the beam can be quite large. This is distinct from a beam line “waist”, corresponding to a narrow part of the beam where the particles are parallel.

### 3.2.4 Beam line momentum calibration

The initial muon momentum distribution was measured on a weekly basis using the dependence of the muon rate on channel scaling; this is equivalent to changing the momentum of the channel. Figure 3.3 shows such a distribution and its deconvolved components; muons are generated at the production target, and are then transported by the beam line, which has an approximately Gaussian acceptance. The channel can be calibrated using the “surface muon edge” that is shown on the figure, since it corresponds to muons from the surface of the target that have exactly 29.79 MeV/ $c$  (kinetic energy 4.2 MeV).

Operating at the surface muon momentum is undesirable since the rate is low. Instead the experiment used an average momentum of 29.6 MeV/ $c$  (kinetic energy 4.1 MeV) corresponding to a thin layer close to the production target’s surface. The selected muons will consequently undergo a small amount of multiple scattering inside the production target, which breaks the relationship between the momentum and spin; this depolarisation is evaluated as a systematic uncertainty in Section 9.5.

The beam line was set to a momentum resolution<sup>10</sup> of FWHM 0.7%, which is a factor two smaller than the previous  $P_\mu^\pi \xi$  analysis. This increases the initial beam polarisation, but not by a significant amount.

Figure 3.3 shows a decrease in the number of muons with production target depth. In practice, the exponent of this decrease was left as a free parameter in fits, but is expected to follow a power law

$$\frac{dN}{dR} \sim R^{-1/6}, \quad (3.1)$$

where  $N$  is the number of muons, and  $R$  is the depth. The derivation of Eq. (3.1) is reserved for a footnote<sup>11</sup>.

---

<sup>10</sup>The momentum resolution,  $\Delta p/p$ , is sometimes referred to as the momentum “bite”. In either case the meaning of  $\Delta p$  must be qualified, since there can be confusion between a Gaussian RMS and FWHM.

<sup>11</sup>Reference [34] can be used to explain this behaviour[35]. The range ( $R$ ) of low momentum muons ( $p \lesssim 100$  MeV/ $c$ ) is well modelled by the power law,  $R \sim p^{3.6}$ , so that  $\frac{dp}{dR} = R^{-0.72}$ . Muons are emitted in a uniform direction from pions, so that phase space requirements give the number of muons as,  $\frac{dN}{dp} \sim p^2$ , and again using  $R \sim p^{3.6}$  yields  $\frac{dN}{dR} \sim R^{-0.56}$ . Combining these results gives

$$\frac{dN}{dR} = \frac{dN}{dp} \frac{dp}{dR} \sim R^{-1/6}.$$

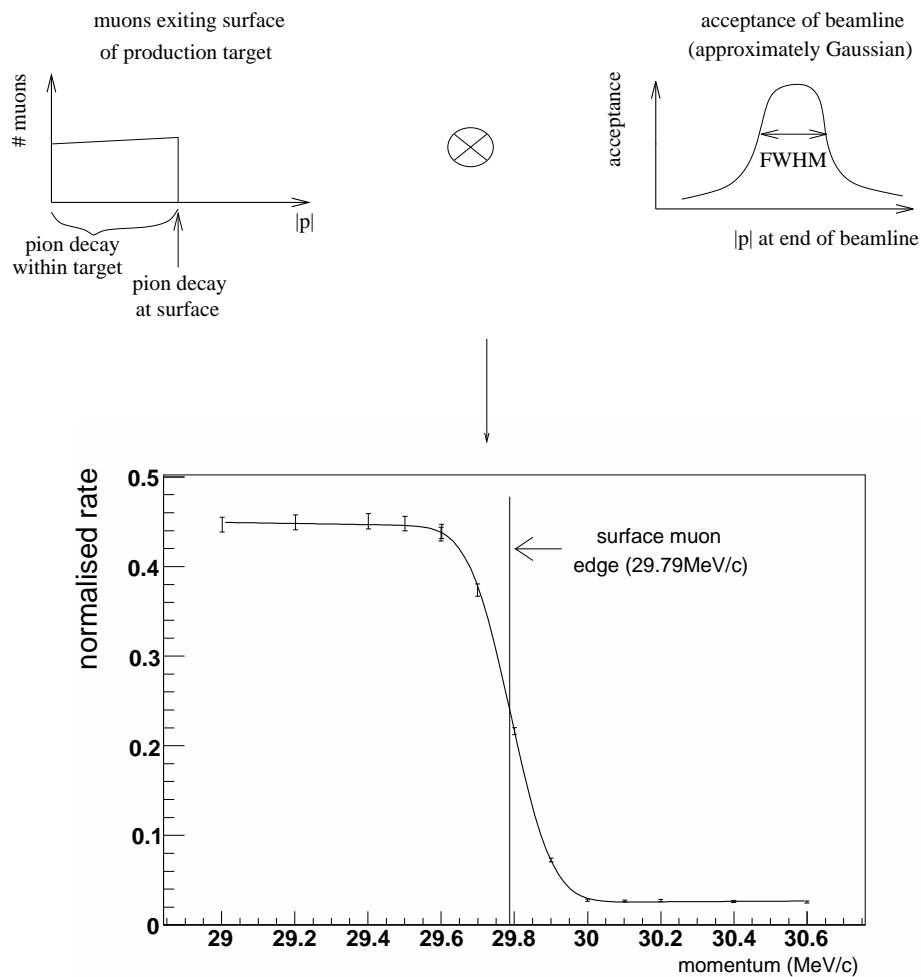


Figure 3.3: In reality, the channel has an approximately Gaussian acceptance (top right), which is convoluted with the momentum distribution from the target (top left). The resulting rate dependence on channel momentum is shown. The “normalised rate” on the ordinate is proportional to muon rate divided by the proton current.

### 3.2.5 Particles delivered

The bending magnet B1 and subsequent slit selected *all* particles with momentum 29.6 MeV/ $c$ . Therefore the desirable surface muons were contaminated with “cloud muons”, “beam positrons”, pions and protons. These contaminations will now be described.

Consider a pion with  $\gamma_\pi$  (velocity  $\beta_\pi$ ); the momentum of the decay muon is given by

$$p'_\mu = \gamma_\pi (p_\mu - \beta_\pi E_\mu), \quad (3.2)$$

where  $p_\mu$  is the muon momentum in the pion rest frame (29.6 MeV/ $c$  for the M13 beam line),  $E_\mu$  is the muon energy in the pion rest frame (109.8 MeV/ $c$ ),  $p'_\mu$  is the Lorentz boosted muon momentum, and  $c = 1$  is assumed. After substituting  $\gamma_\pi^2 = (1 - \beta_\pi^2)^{-1}$  into Eq. (3.2), the result is a quadratic equation in  $\beta_\pi$ ,

$$[E_\mu^2 + (p'_\mu)^2] \beta_\pi^2 - [2p_\mu E_\mu] \beta_\pi + [p_\mu^2 - (p'_\mu)^2] = 0, \quad (3.3)$$

which can be solved to give

$$\beta_\pi = \frac{p_\mu E_\mu \pm \sqrt{p_\mu^2 E_\mu^2 - [E_\mu^2 + (p'_\mu)^2] [p_\mu^2 - (p'_\mu)^2]}}{E_\mu^2 + (p'_\mu)^2}. \quad (3.4)$$

For the case  $p_\mu^2 = (p'_\mu)^2 = 29.6 \text{ MeV}/c$  there are now two solutions:  $\beta_\pi = 0$  for a stationary pion, corresponding to the surface muons that the experiment wants to accept, and

$$\beta_\pi = \frac{2p_\mu E_\mu}{E_\mu^2 + (p'_\mu)^2} = 0.503, \quad (3.5)$$

which using  $p = mv\gamma$  corresponds to a pion with momentum 81.2 MeV/ $c$ . The muons from these pion decays are referred to as “cloud muons”; they originate from pions moving between the production target and B1 that decay with a muon in the direction *opposite* to their motion. This decay must occur before the pion reaches the momentum selection at B1, and is therefore prompt. These muons will have opposite polarisation to the surface muons, and therefore must be removed with confidence. Since they are prompt, this can be achieved by a conservative time of flight cut.

The contamination of “beam positrons” mainly originates from muon decays within the production target<sup>12</sup> and surrounding materials. There are also contributions from neutral

---

<sup>12</sup>Prior to the current measurement, data had been acquired using a Beryllium production target encased in a steel jacket. This had a high beam positron rate due to muons stopping and decaying in the steel jacket.

pion decays ( $\pi^0 \rightarrow \gamma\gamma$ ) since the  $\gamma$ 's shower in the production target and beam pipe. The trigger scintillator was set to mostly ignore positrons, but they are high rate and therefore still produce a significant background in muon-triggered events. The event reconstruction software was readily able to remove the beam positron trajectories, since they pass through the entire detector.

The proton contamination was removed by a beam line window, and the pion contamination could be separated by time of flight due to their heavier mass<sup>13</sup>. A typical time of flight spectrum is shown in Fig. 3.4.

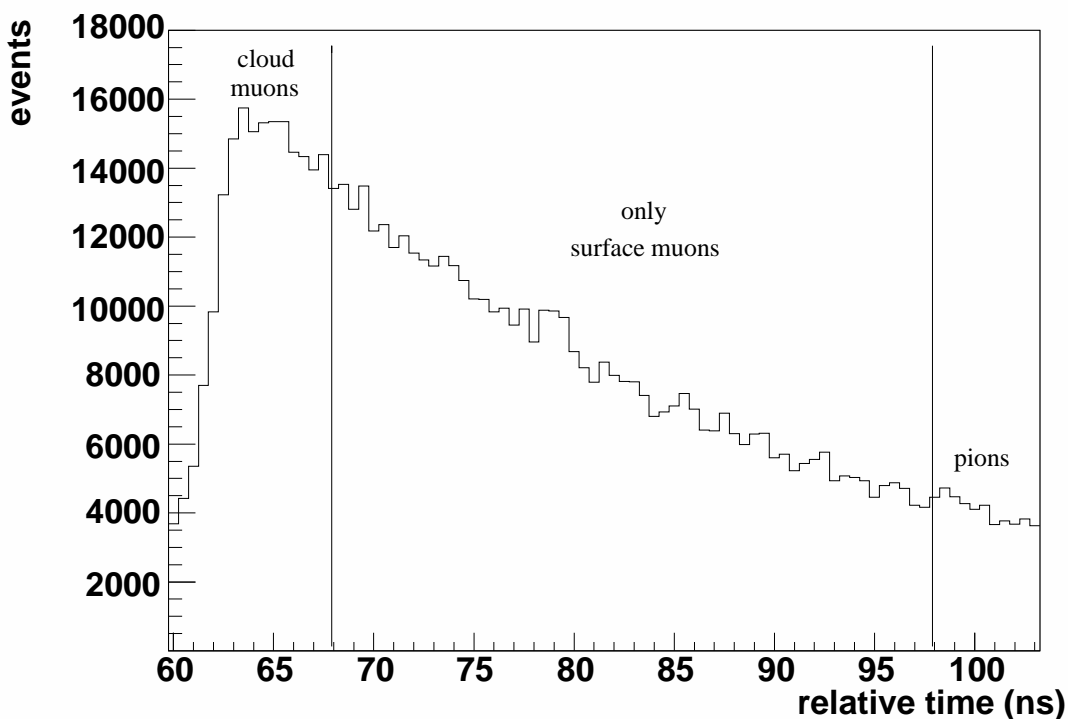


Figure 3.4: The relative time of flight for trigger particles during one period of the cyclotron (43 ns) is shown, as used to select surface muons. Cloud muons can be rejected since they are prompt. Pions can be removed since they take longer to traverse M13 due to their larger mass. Protons are not shown since they don't make it to the trigger. Positrons are not shown since the trigger scintillator has low sensitivity to them.

---

This is one of the reasons the experiment used a graphite target for the data acquisition described in this thesis.

<sup>13</sup>The experiment has observed the decay  $\pi^+ \rightarrow \mu^+\nu_\mu$ , by selecting pions using their time of flight and pulse height in the trigger scintillator. However the statistics were too low to make a publication quality measurement, and the detector is blind to the decay mode  $\pi^+ \rightarrow \mu^+\nu_\mu\gamma$ , which is a radiative correction that is significant when attempting a competitive measurement of the ratio  $\pi^+ \rightarrow \mu^+\nu_\mu$  to  $\pi^+ \rightarrow e^+\nu_e$ .

### 3.2.6 M13 configurations

Alignment and calibration runs used different M13 settings. For example, drift chamber alignment used higher momentum pions, and calibration of the time expansion chambers used a spread muon beam. An entire data set was taken at a lower momentum of 28.9 MeV/ $c$  as a consistency check. The special configurations and sets are described in more detail in Section 8.4.

## 3.3 Measuring the muon beam

The final polarisation of the muons must be known with high precision. Ideally this would be measured using the velocity vector inside the detector. However, this would be technically challenging since the detector is within a 2 T magnetic field (see Section 3.7). Instead the muon beam is measured at the end of the M13 channel, before the muons have encountered significant material or magnetic field. At this point, the muon beam has encountered a small amount of material, so that a muon's momentum and spin vectors are opposite to an acceptable approximation. The muons can then be simulated to determine their final polarisation.

In 2002, measurements of the muon beam were made using a wire chamber. Other experiments have simply used a scintillator[15]. However, the systematic uncertainty goal for  $P_{\mu}^{\pi} \xi$  meant that a more precise method was needed. Prior to accumulating data in 2004, a pair of identical time expansion chambers<sup>14</sup> were constructed to measure individual muon trajectories with high precision. These chambers started to be used in 2004, when the experiment's original  $P_{\mu}^{\pi} \xi$  measurement was carried out. The first time expansion chamber (TEC) module measured  $x$  and  $\theta_x$ , and the second module measured  $y$  and  $\theta_y$ . In order to minimise multiple scattering while measuring the trajectory, the mass of the system was kept as low as possible. Despite these efforts, the multiple scattering of the TECs meant they could not remain in place during nominal data acquisition. Therefore the modules were inserted on a weekly basis for approximately an hour of beam measurements. The alignment and calibration of the TEC modules is described in Sections 3.14 and 3.16. The analysis of the data from the TECs is detailed in Chapter 5.

The positioning of the box containing the modules is shown in Fig. 3.5. The TEC modules are located close to the F3 focus, where the beam has a small extent. When the muon beam

---

<sup>14</sup>A time expansion chamber is a type of time projection chamber. The drift volume is divided into a low electric field region separated from a higher field amplification region. The result is a higher precision measurement.

encounters the TECs, it has passed through no material except for a single thin ( $6\ \mu\text{m}$  Mylar) beam line window. The low magnetic field means that trajectories are well approximated by straight lines, which simplifies the analysis.

The TEC modules are labelled “X Module” and “Y Module” in Fig. 3.6. Each module is  $8.0\ \text{cm}$  long with an active area of  $6.0\ \text{cm} \times 6.0\ \text{cm}$ . They are inside a box that is filled with low pressure ( $8\ \text{kPa}$ ) Dimethylether<sup>15</sup> gas that constantly flows at a rate of  $100\ \text{cm}^3/\text{min}$ . An electric field is maintained over the drift volume by a graded voltage applied to drift wires, as shown in Fig. 3.7. Charged particles ionise the gas, and this ionisation drifts towards the sense plane. The electrons enter a high field region, separated by grid (“guard”) wires. In the high field “multiplication region” the electrons are accelerated towards small diameter ( $25\ \mu\text{m}$ ) sense wires where they avalanche and cause a signal. The time of signal relative to the muon trigger is then converted into a distance using space-time relationships (STRs). Each TEC had 24 sense wires at  $0.2\ \text{cm}$  pitch. Thicker shield wires were placed between the sense wires to ensure the avalanches remained localised.

The electric field in the drift volume was nominally uniform with strength  $16\ \text{V}/\text{mm}$ . However the field is non-uniform by up to  $10\%$  due to the field at the sense planes leaking into the drift volume, and by  $\sim 1\%$  due to modular interference[30]. Ultimately the non-uniformity in the electric field is addressed by iterating the STRs using real tracks.

---

<sup>15</sup>This gas was chosen since it was already in use in the drift chambers. See Section 3.8 for the advantages of Dimethylether.

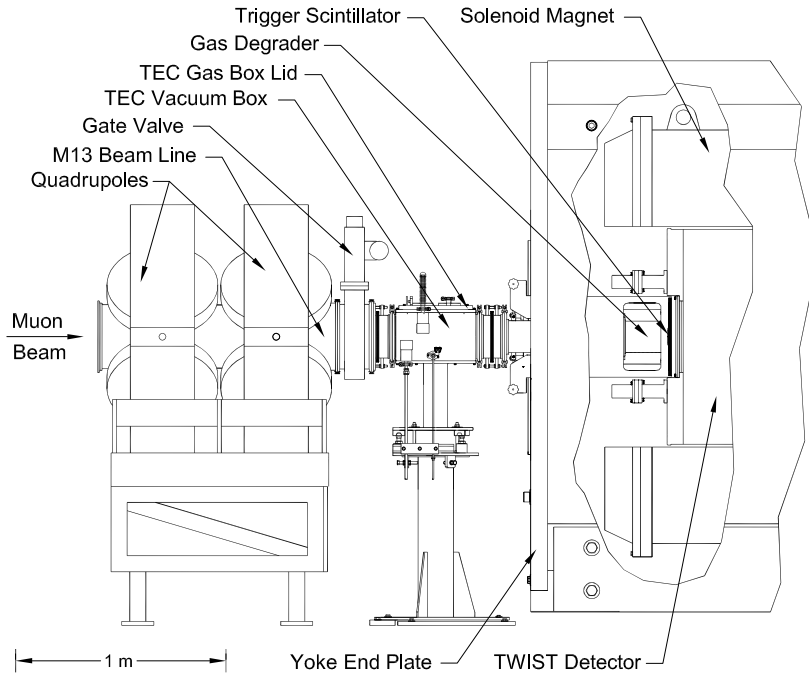


Figure 3.5: The positioning of the time expansion chambers relative to the M13 beam line and solenoid. This is Fig. 1 from Ref. [30].

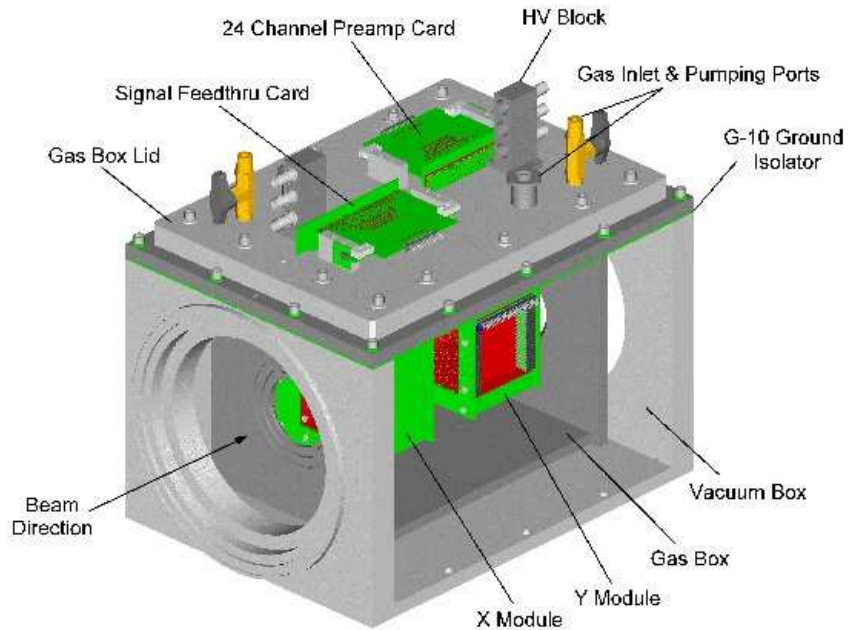
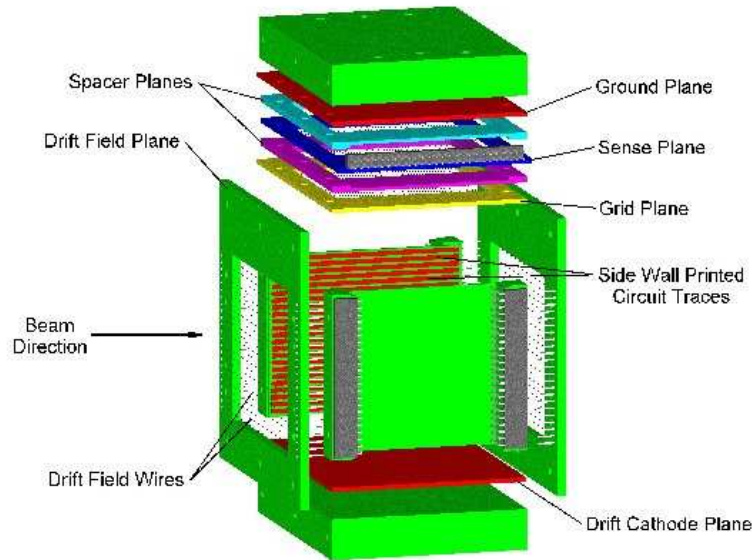
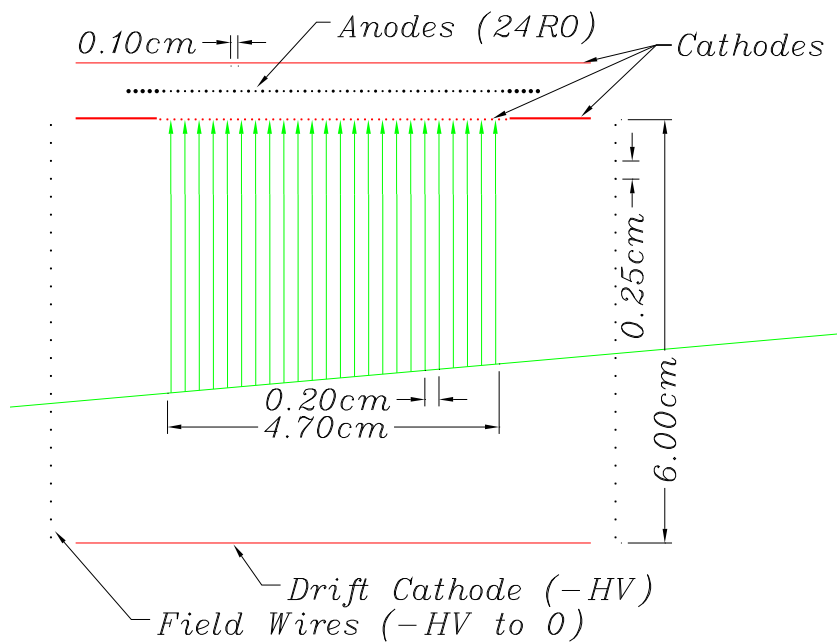


Figure 3.6: The location of the time expansion chamber modules and their electronics is shown. This is Fig. 2 from Ref. [30].



(a) Components of a single time expansion module. This is Fig. 3 from Ref. [30].



(b) Cross section through a single time expansion module, with dimensions shown. The initial ionisation is indicated by the green line through the entire module. The green arrows show the direction of the drift electrons. This is Fig. 2.13 from Ref. [36].

Figure 3.7: An individual time expansion chamber module.

### 3.4 Quadrupole steering

In the previous  $P_\mu^\pi \xi$  analysis the muon beam was found to be approximately 1 cm too high at the TECs, with a non-zero average  $y$ -angle, which resulted in a larger depolarisation than the design specification. The deflection is blamed on an interference between the solenoid's fringe field and the final M13 quadrupole[30]. The dipole magnets only steered horizontally, so were not able to correct for this deflection. A major improvement for the current  $P_\mu^\pi \xi$  measurement was a correction of the deflected beam by applying additional currents to the poles of the M13 quadrupole magnets<sup>16</sup>.

The left hand side of Fig. 3.8 demonstrates the behaviour of an unmodified vertically focusing quadrupole magnet. In the vertical direction the charged particles are focussed, and in the orthogonal horizontal direction the particles are defocussed. If the poles of the quadrupole are asymmetrically excited using additional current sources then "The effect ... is to shift the field zero to a new location"[37] and a charged beam is both focussed and steered. For example, the right hand side of Fig. 3.8 shows current sources added to two of the poles, resulting in a horizontal steering force.

There have been theoretical calculations of the steering effect[37]. However, since the experiment is able to precisely measure the muon beam after the quadrupoles and before the detector's fringe field, no theoretical predictions were made and the beam was simply observed while increasing currents were applied to the pole(s) of accessible quadrupole magnets.

Five power supplies were available to be placed over the poles of Q4, Q6 and Q7. Q6 and the dipole magnet B2 were used to steer horizontally. Q4 and Q7 were used to steer vertically, with Q4 providing most of the steering. The response of the beam's average position ( $\langle x \rangle, \langle y \rangle$ ) and angle ( $\langle \theta_x \rangle, \langle \theta_y \rangle$ ) were determined by steering with each element separately. While attempting to steer primarily in the  $x$  or  $y$  direction, all four parameters of the beam were changed. For example, Fig. 3.9 shows that when primarily steering horizontally, there is a second order beam movement in the vertical direction.

Relationships such as Fig. 3.9 were determined for each quadrupole. Fortunately the response was almost always linear, and assuming the beam's response won't change as the

---

<sup>16</sup>Using quadrupoles to deflect a charged particle beam is not a new technique. Prior to installation in M13, it was already in use in the TRIUMF proton beam line. Also new beam lines such as  $\mu E4$  at PSI are being constructed with quadrupole steering as part of the design[15].

beam is steered, the results can be combined according to

$$\begin{pmatrix} \langle x \rangle' \\ \langle y \rangle' \\ \langle \theta_x \rangle' \\ \langle \theta_y \rangle' \end{pmatrix} = \begin{pmatrix} \langle x \rangle \\ \langle y \rangle \\ \langle \theta_x \rangle \\ \langle \theta_y \rangle \end{pmatrix} + \begin{pmatrix} r_x^{B2} & r_x^{Q6} & r_x^{Q4} & r_x^{Q7} \\ r_y^{B2} & r_y^{Q6} & r_y^{Q4} & r_y^{Q7} \\ r_{\theta_x}^{B2} & r_{\theta_x}^{Q6} & r_{\theta_x}^{Q4} & r_{\theta_x}^{Q7} \\ r_{\theta_y}^{B2} & r_{\theta_y}^{Q6} & r_{\theta_y}^{Q4} & r_{\theta_y}^{Q7} \end{pmatrix} \begin{pmatrix} \Delta B2 \\ I_6 \\ I_4 \\ I_7 \end{pmatrix},$$

where the primed quantities are the final beam parameters,  $\Delta B2$  is the change in B2's magnetic field, and the  $I$  terms refer to the additional currents applied to the quadrupoles. The  $r$  quantities are the gradients of relationships such as Fig. 3.9, where the subscript refers to the beam parameter and the superscript refers to the steering element. For example,  $r_x^{Q6}$  and  $r_y^{Q6}$  are the gradients in Fig. 3.9. The beam tuning criteria will be described later in the thesis.

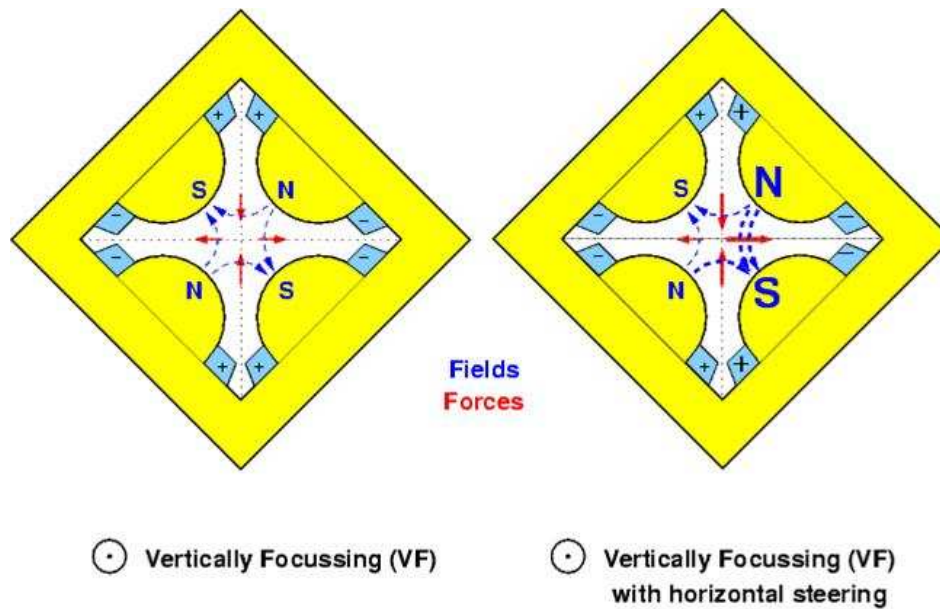


Figure 3.8: An unmodified vertically focusing quadrupole is shown on the left. The same quadrupole with asymmetrically excited poles is shown on the right. The modified quadrupole both focusses and deflects the beam.

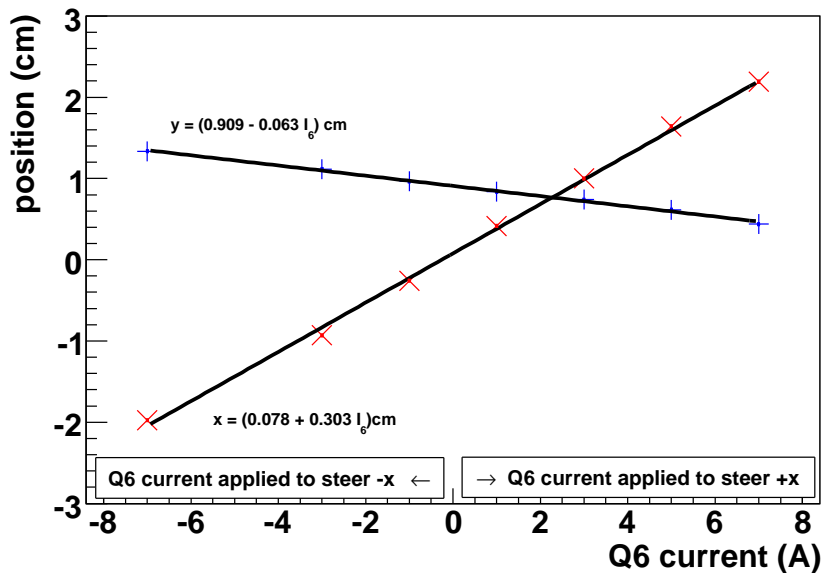


Figure 3.9: The response of the muon beam to changes in the horizontal steering of Q6.

### 3.5 The detector

The detector was fully constructed and had been working for four years when the author commenced studies. Therefore only a summary of the detector will be given here, especially as this topic is covered in detail elsewhere [29][36][38]. A schematic of the apparatus is shown in Fig. 3.10. The essential features are a superconducting magnet with iron yoke, a stack of proportional and drift chambers (“the stack”), and a muon stopping target at the centre. For simplicity, the figure does not show the material upstream and downstream of the stack. Muons enter the detector and are stopped in the high purity metal target. The decay positron spirals in the magnetic field, leaving ionisation in the chambers. This allows the positron’s position to be measured and trajectory reconstructed, from which the initial energy and angle can be inferred.

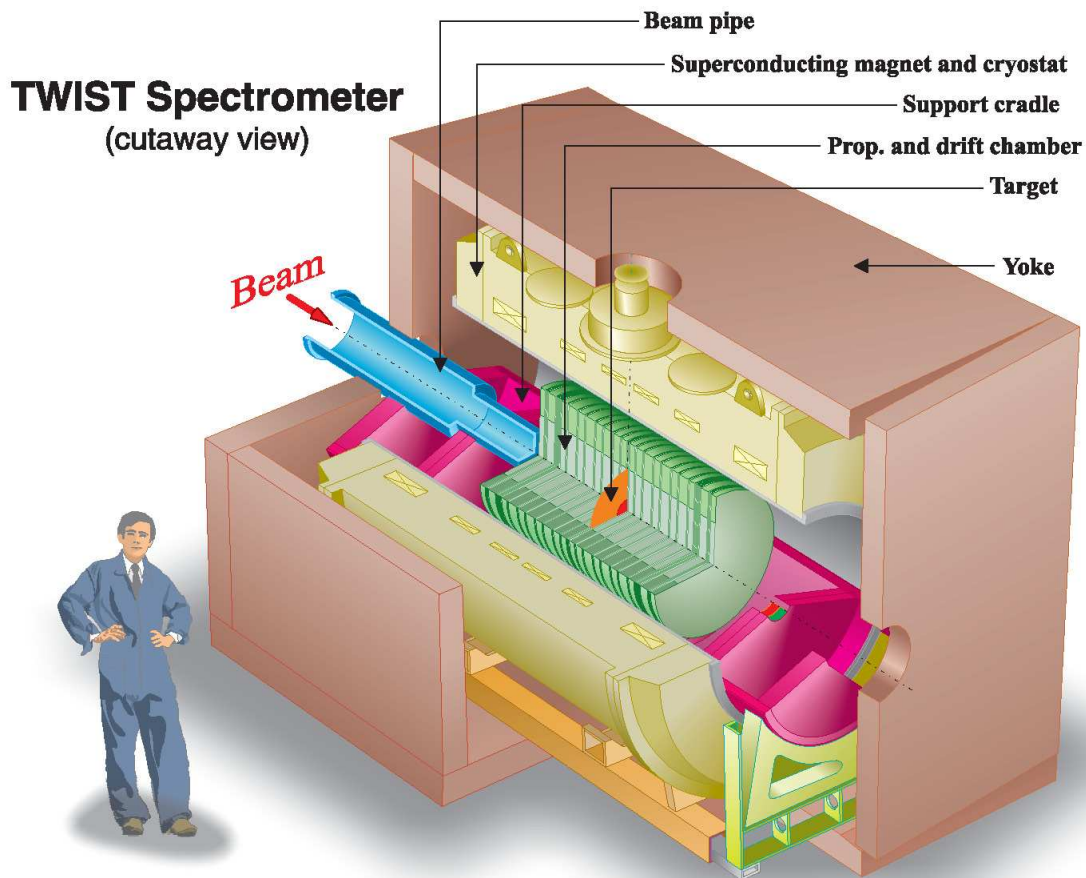


Figure 3.10: Schematic of the detector.

### 3.6 Coordinate system

The longitudinal direction,  $z$ , is along the beam line axis shown in Fig. 3.10 and the  $y$  direction is vertical.  $z$  is positive in the beam direction (“downstream” direction), and  $z = 0$  is defined to be half way between the wire planes of the central proportional chambers<sup>17</sup>. As will be described in Section 3.8, the wire chambers are inclined at  $45^\circ$  with respect to the vertical, and this rotated system is described by  $u$  and  $v$  coordinates.

In terms of decay positrons,  $\theta$  is measured with respect to the  $z$ -axis, so that ( $0 < \cos \theta < 1$ ) corresponds to upstream decays, and ( $-1 < \cos \theta < 0$ ) to downstream decays. This is shown graphically in Fig. 3.11.

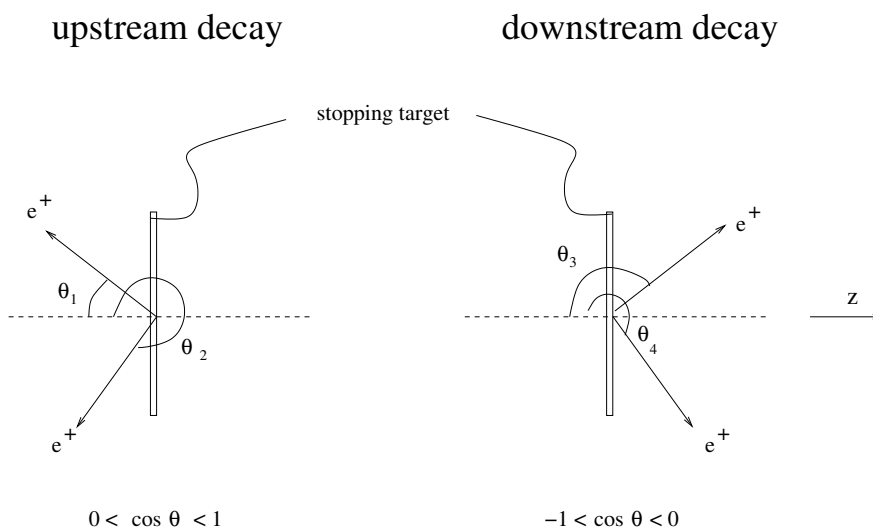


Figure 3.11: In the experiment’s coordinate system,  $\cos \theta > 0$  corresponds to an upstream decay, and  $\cos \theta < 0$  to a downstream decay.

### 3.7 Solenoid

The solenoid and surrounding iron yoke were shown in Fig. 3.10. The solenoidal magnetic field was needed for the following reasons:

1. Inside the solenoid, where the field is strong (nominally 2 T), uniform, and longitudinal ( $z$ ), the decay positrons will spiral, with the radius and pitch angle related to the positron momentum and decay angle.

<sup>17</sup> $z = 0$  is not quite the location of the metal stopping target. See Section 3.11.

2. While muons are inside the target, the strong field holds their spin against depolarisation from the nuclear dipole moments. Any Muonium formation in the gas immediately before the target is suppressed by the field.
3. In the fringe field region upstream of the detector's chambers, the field radially focuses the muon beam, which maintains a high polarisation with respect to the  $z$ -axis.

The field was provided by a liquid helium cooled superconducting solenoid manufactured by Oxford Magnet Technologies Limited (UK). The magnet was originally part of medical apparatus used for magnetic resonance imaging<sup>18</sup>.

In the case of an infinitely long solenoid, the field inside would be perfectly uniform. However the experiment's superconducting solenoid had a bore of diameter 1.05 m, and a length of only 2.23 m, resulting in significant departures from uniformity. For this reason the magnet had doors of high permeability steel at both ends (visible in Fig. 3.10), at which the field lines must be close to perpendicular, resulting in increased uniformity through the central region. The thickness of the doors (8 cm) was carefully chosen to maximise uniformity. Each door had a 40 cm diameter circular hole that detracts from the field uniformity<sup>19</sup>. The doors were part of a custom built iron "yoke" with square cross-section of side 3 m and thickness 0.20 m, which provided an easy return path for the magnetic flux. The yoke limits the solenoid's fringe field in the  $z$ -direction, minimising interference with the beam line, and allowing the experiment to measure the muons after the beam line, but before the magnetic field. This can all be seen in Fig. 3.12, where the direction of the magnetic field lines are shown in blue, and the red contours indicate the magnitude of the field.

The strength of the field dictates the range of positron helix radii that can be reconstructed. The nominal<sup>20</sup> value for maximum field was  $B = 2$  T, but sets were also taken at  $B = 1.96$  T and  $B = 2.04$  T as a consistency check. The strength of the magnetic field decreased by 0.02 mT over a period of approximately 3.5 months[39]. The field strength was continuously measured using an NMR probe just outside the tracking region. The change in magnetic field is corrected for in the analysis by scaling the magnetic field used to analyse each set.

---

<sup>18</sup>The magnet is no longer at TRIUMF. In September 2008 it was transported to Michigan State University, home of the National Superconducting Cyclotron Laboratory.

<sup>19</sup>The extent of the muon beam is  $\sim 5$  cm, yet the holes in the door are 40 cm. There are two reasons for this: the trigger and light guides required a significant amount of space, and the muon beam will be less sensitive to imperfections in the doors' steel if it is further from the hole's boundary.

<sup>20</sup>Ideally the field would have been a little higher to recover positrons with larger transverse momentum. However early experience with the solenoid suggested the forces on the coils became a concern for  $B > 2.04$  T.

The transverse and longitudinal components of the field are shown in Fig. 3.13. In the analysis particles are no longer tracked or simulated if their radii is greater than 20 cm. Therefore the  $r = 30$  cm line is only included to demonstrate the field extremes. The figures show that the field is weak but non-zero for  $z \approx -192$  cm, corresponding to the time expansion chambers that measure the muon beam. The transverse field components at off-axis positions increase until  $z \approx -140$  cm, at which point the  $z$  position is within the yoke and these components start to decrease. The inset tracking region corresponds to the area occupied by the drift chambers. There are proportional chambers slightly upstream (and downstream) of this region. The uniformity inside the tracking region is clearly very high.

The field was measured at  $B = 1.96$  T,  $B = 2.00$  T and  $B = 2.04$  T using the custom built apparatus shown in Figs. 3.14. and 3.15. Hall probes were placed along an arm at intervals of 4.13 cm, and the apparatus was rotated by  $15^\circ$  increments and moved in steps of 5 cm or 2.5 cm longitudinally<sup>21</sup> ( $z$ ). The Hall probes only measured the longitudinal component of the field, and were calibrated using NMRs that measured the total field. The Hall probe measurements were accurate to 0.1 mT. In 2002 measurements were taken of the tracking region using seven probes on the rotating arm. In 2003 measurements of the fringe field and the upstream part of the tracking region were taken. For the 2003 measurements only five Hall probes were used since the assembly needed to pass through the hole in the doors.

A simulation was required to smooth out the field and generate the  $x$  and  $y$  components. The OPERA software package[40] was used for this purpose. The measurements taken with the Hall probe mapper were not given to OPERA. Instead the pieces shown in Fig. 3.16 were modelled, and their positions and magnetic properties adjusted to minimise the differences between OPERA and the measurements. A number of Summer students modified the coil positions, current density, coil radii, material B-H curves and door position to minimise this difference. The final OPERA map matches to 0.2 mT within the 2 T region. Further upstream, the match becomes worse as demonstrated in Fig. 3.17.

---

<sup>21</sup>The smaller steps were taken at the edges of the tracking region.

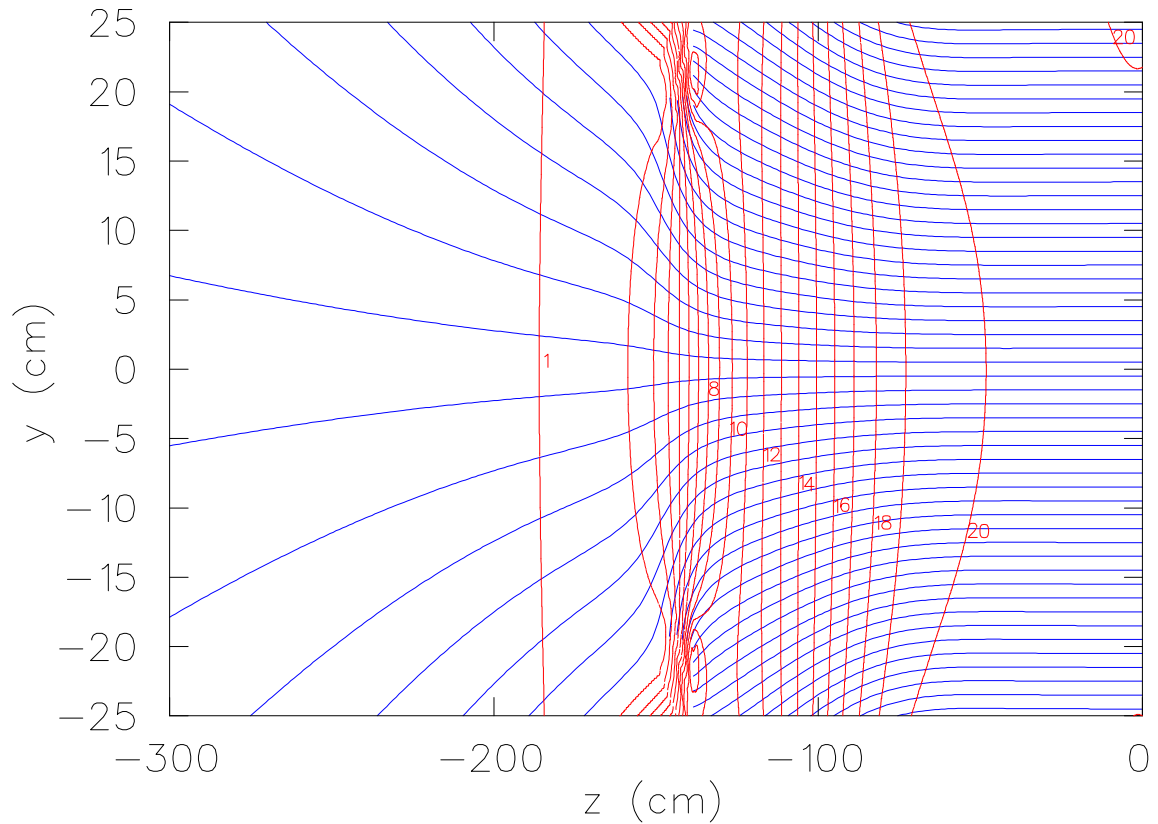
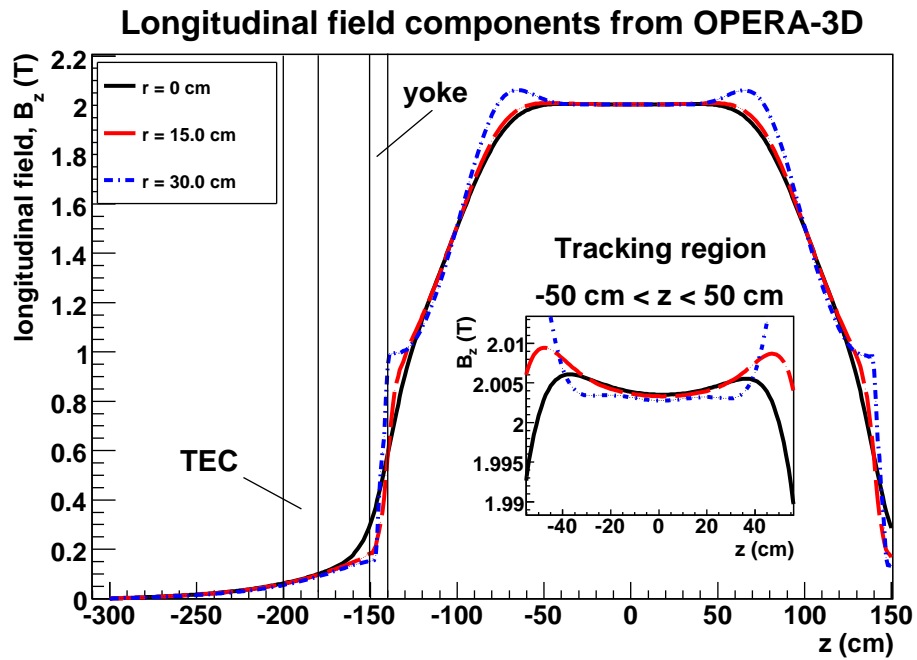
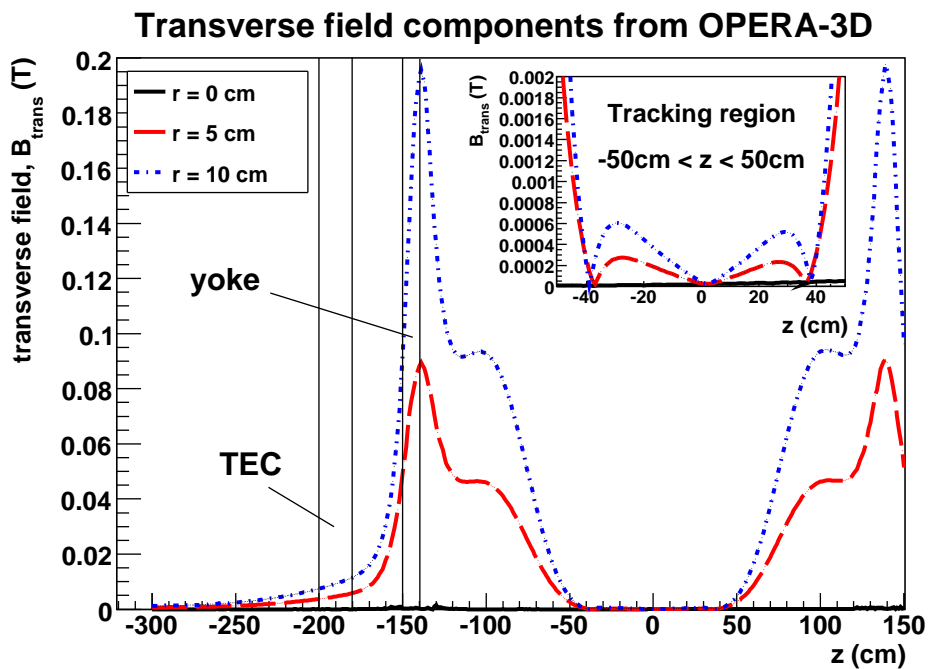


Figure 3.12: The magnetic field for  $x = 0$ . The blue lines indicate the direction of the magnetic field vector. The red contours indicate the field strength in kG. The line 20 kG corresponds to 2 T. The scales on the ordinate and abscissa differ significantly. This is a simplified version of a figure supplied by Glen Marshall.



(a) Longitudinal components of the magnetic field map.



(b) Transverse components of the magnetic field map.

Figure 3.13: Components of the OPERA magnetic field map.

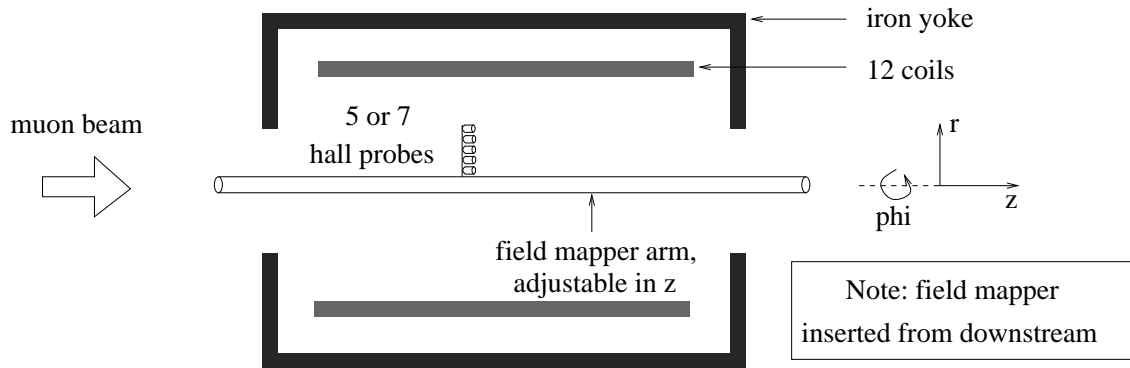


Figure 3.14: The field mapper is shown schematically. Hall probes were attached at radial intervals of 4.13 cm, and the arm was rotated in  $15^\circ$  increments. The whole assembly could be moved longitudinally.



Figure 3.15: A photograph of the field mapper, taken from inside the solenoid. The bore of the magnet has 1 m diameter.

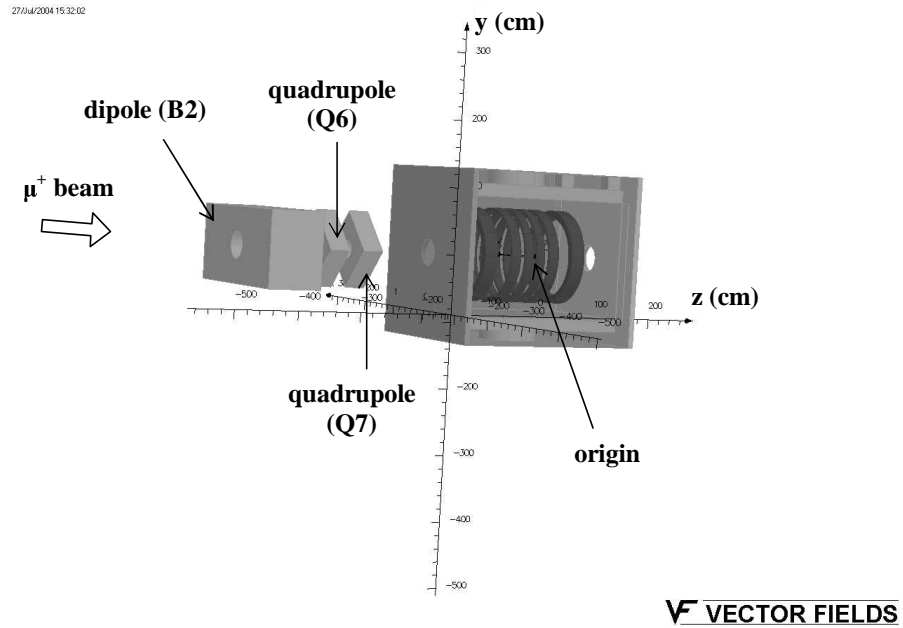


Figure 3.16: Components included in the OPERA simulation of the magnetic field.

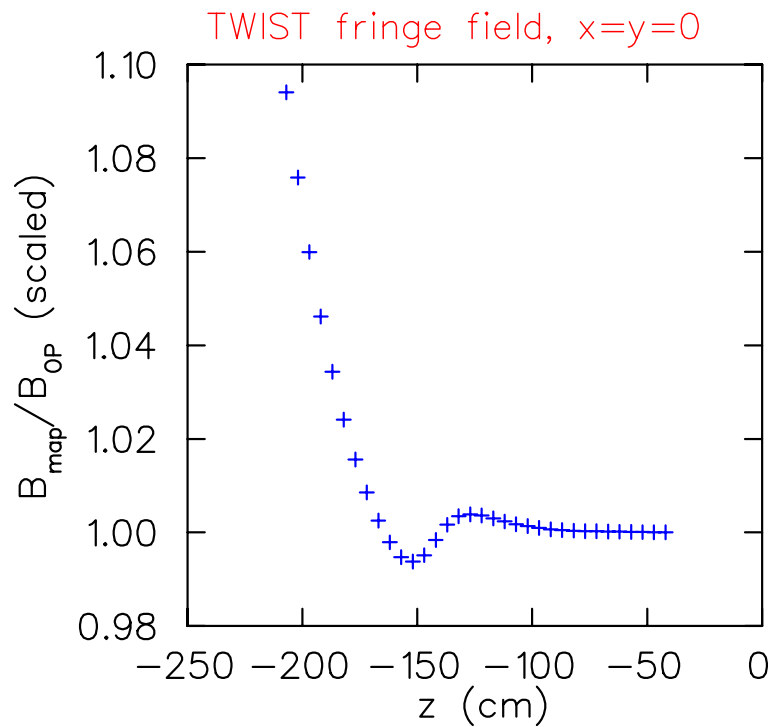


Figure 3.17: For  $x = y = 0$ , the ratio of the measured field map to the OPERA model. Figure produced by Glen Marshall.

### 3.8 Wire chambers

The 120 cm detector stack included 44 multi wire drift chambers and 12 multi wire proportional chambers, which are shown in Fig. 3.18, and will now be referred to as DCs and PCs. The construction of the DCs and PCs is very similar, and a chamber is shown schematically in Fig. 3.19. Wires of diameter  $15\ \mu\text{m}$  are placed at pitches of 0.4 cm (DCs) and 0.2 cm (PCs), with a total of 80 wires per plane for the DCs, and 160 wires per plane for the PCs. All of the DC wires were individually instrumented, but the outer wires of the PCs were joined together in groups of four and then readout<sup>22</sup>. The cathodes (which served as gas windows) for each chamber were constructed from  $6.35\ \mu\text{m}$  thick Mylar foil, which was aluminised on both sides to allow conduction<sup>23</sup>. The cathode-to-cathode distance was 0.4 cm. The emphasis is on low mass, to minimise scattering and energy loss, which ultimately improves the reconstruction of positron trajectories. A pair of proportional chambers is just  $1 \times 10^{-4}$  radiation lengths[41]. The low mass is also important for the muons since at  $p_\mu = 29.6\ \text{MeV}/c$  their range is  $140\ \text{g}/\text{cm}^2$ , which is equivalent to roughly 0.1 cm of water.

The DCs and PCs were filled with different gases. The DCs measured the position of ionising particles with high precision, and the experiment filled the chambers with Dimethylether (DME) gas. This has a number of desirable properties[42]: the number of clusters per cm is high ( $30\ \text{cm}^{-1}$ ), the drift velocity is small ( $2.5\ \text{cm}/\mu\text{s}$ ), and the Lorentz angle between the electric field and electron drift velocity is small ( $5^\circ$ ). The DC response times were  $\sim 10^2\ \text{ns}$ , and the efficiency was  $> 99.95\%$ [29]. The PCs were used to separate particles in time and differentiate between muons and positrons using pulse width. They were filled with a mixture of  $\text{CF}_4$  and Isobutane, a combination with a high drift velocity. This allowed response times  $\lesssim 20\ \text{ns}$ . Proportional chambers were chosen over scintillators to minimise material, cover a large area, and operate efficiently in the experiment's strong magnetic field. Unfortunately a proportional chamber could not be used as the trigger since the time resolution is insufficient to separate cloud muons from surface muons; instead a dedicated trigger scintillator was used, which is described in Section 3.10.

Between the chambers a mixture of helium and nitrogen in the ratio 97:3 was used. The helium minimised material, and nitrogen prevented sparking<sup>24</sup>. The helium and nitrogen

---

<sup>22</sup>The availability of TDCs (time to digital converters) limited the instrumentation of the PCs. The chosen instrumentation was adequate since the spatial distribution at the PCs was only used to select muons close to the target, and these wires *were* individually instrumented.

<sup>23</sup>The Mylar foils were doubly aluminised regardless of whether they were exposed to chamber gas or the helium/nitrogen mixture. This was done simply for uniformity.

<sup>24</sup>The cross section for electrons in pure helium is very small, allowing a long mean free path. Hence the electron can accelerate and ionise, eventually causing a spark. The nitrogen significantly reduces the mean free path, and therefore minimises sparking.

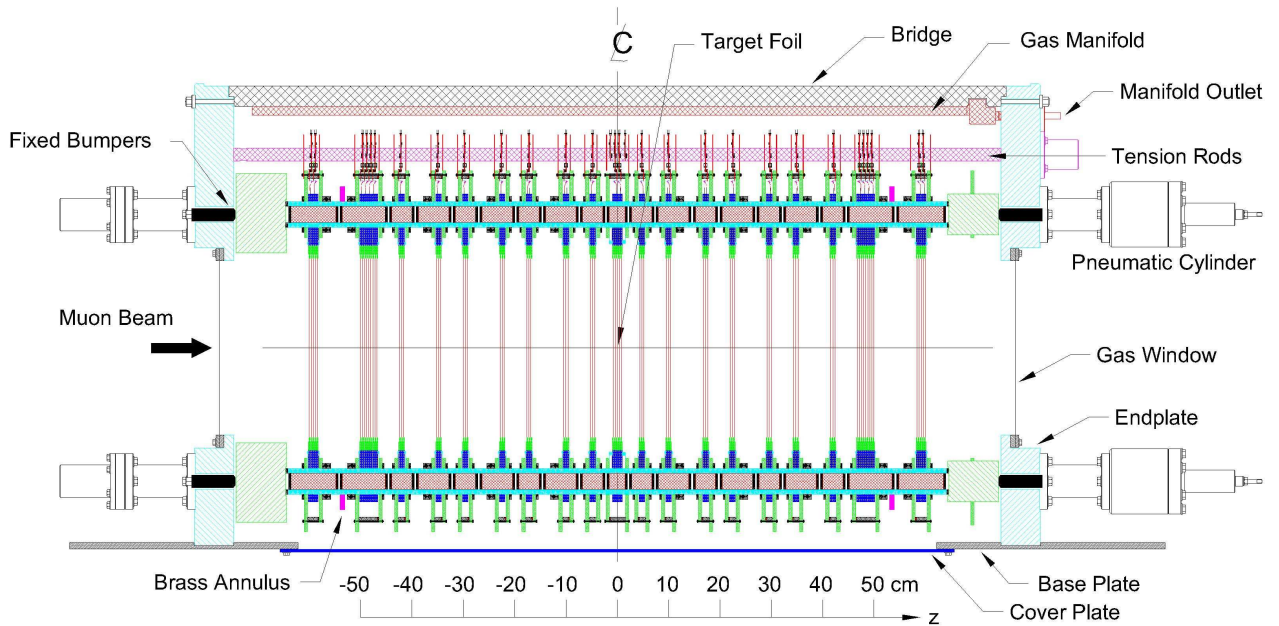


Figure 3.18: Side view of the detector.

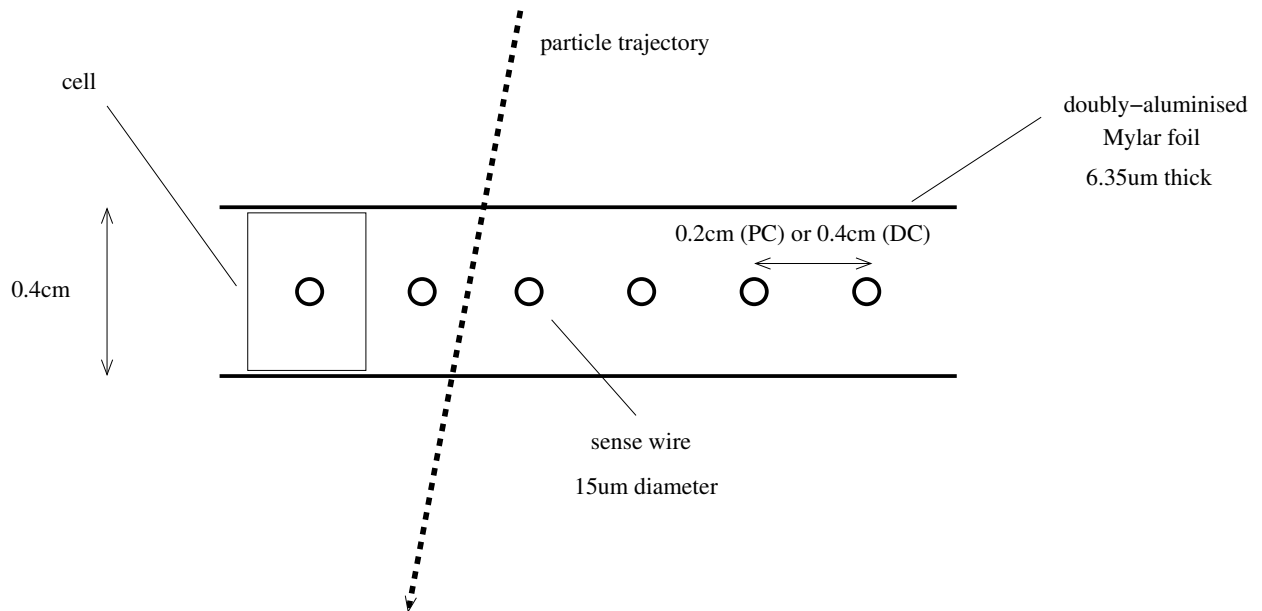


Figure 3.19: Schematic of a wire chamber. Both the DCs and PCs have cathodes of Mylar coated with aluminium; these also act as gas windows. The cathode-to-cathode distance was always 0.4 cm.

were constantly flowed, allowing the electrostatic bending of the thin cathode foils to be counteracted. The gases inevitably leaked through cathode foils, so that a constant flow was needed to maintain purity. The gas system had to be vented to atmosphere, requiring a fast response to changes in atmospheric pressure and room temperature. The differential pressure between the He/N mix and the drift chambers had to be maintained to 4 mTorr[36].

The chambers were assembled into modules with shared cathodes. In the simplest case two planes were orthogonal with a single shared cathode. These two plane modules were used in the region  $-45.0 \text{ cm} < z < 45.0 \text{ cm}$  in Fig. 3.18, and made up the “sparse stack”. There were also two “dense stacks” of eight DCs, where the seven internal cathodes were shared. At the beginning and end of the detector there were four plane modules of proportional chambers. The module containing the stopping target used the target’s material as a shared cathode. For all modules the wire planes were inclined at  $45^\circ$  with respect to the vertical, and the rotated system was described by  $u$  and  $v$  coordinates, rather than  $x$  and  $y$ . The rotation allowed the electronics to be placed at the same position on each plane, and made the gravitational sag the same in  $x$  and  $y$ .

For 2006/7 the voltage on the two PCs immediately before the stopping target were reduced. The resulting pulse widths were sensitive to the muon’s energy loss, allowing muons that stopped before the metal target to be rejected.

Figure 3.18 shows the detector is symmetric in  $z$  about the central muon stopping target. The modules were positioned in  $z$  using ceramic spacers provided by the experiment’s Russian collaborators. The material was “Sitall CO-115M”, which has a coefficient of linear thermal expansion of just  $\sim 1 \times 10^{-7}(dL/L)/^\circ C$ [29]. For comparison, the coefficients of diamond and carbon steel are  $1 \times 10^{-6}(dL/L)/^\circ C$  and  $11 \times 10^{-6}(dL/L)/^\circ C$ . respectively. The material is strong and had surfaces that were flat and parallel to  $< 0.5 \mu\text{m}$ [29]. The spacers were 0.4 cm for the chambers, and 2.0 cm or 4.0 cm for spacing between the modules. The  $z$  position was maintained by four pneumatic cylinders, which are indicated in Fig. 3.18, and these exerted 1470 N on the stack. The length of the detector assembly was measured “with a precision considerably better than  $50 \mu\text{m}$ ” so that the “relative position of each 4 mm Sitall in the stack is known with a precision of a few microns”[29].

### 3.9 Muon ranging

The positioning and quantity of material encountered by the surface muons is essential to the experiment's success. As previously mentioned, their total range is about 0.1 cm of water, and for a muon stopping distribution that is centred in the target, their kinetic energy must be reduced from 3 MeV to 1 MeV. There must be no significant material before the solenoidal fringe field, since multiple scattering increases the beam emittance, which results in a reduced final polarisation.

The materials seen by muons stopping in the target are summarised in Table 3.1; the next section will describe the materials prior to the DCs and PCs. A simple summation of thicknesses, which is acknowledged to be imperfect, suggests the muons see between 138 mg/cm<sup>2</sup> and 175 mg/cm<sup>2</sup> of material, which can be roughly compared to the surface muon ( $p = 29.79$  MeV/c) range of 143 mg/cm<sup>2</sup> of carbon. In the previous  $P_{\mu}^{\pi} \xi$  measurement, the simulation used incorrect thicknesses for the upstream gas degrader window (79.3  $\mu$ m instead of 93.0  $\mu$ m), and the muon scintillator (195  $\mu$ m instead of 240  $\mu$ m)<sup>25</sup>. As a consequence, the simulation required an extra 12.8 mg/cm<sup>2</sup> of material to match the data stopping distribution[36]. Since the current thesis describes the final measurement, the apparatus was disassembled and materials re-weighed. The simulation now only requires an extra 1.9 mg/cm<sup>2</sup> of material, implemented by adding 13  $\mu$ m of Mylar. This is within the uncertainties from the unsimulated bulge in the vacuum window (1.0 cm, which is  $\approx 1.0$  mg/cm<sup>2</sup> of extra gas), uncertainties in other material thicknesses (stopping target, cathode foil, cathode foil bulges), and uncertainties in modelling the energy loss for highly ionising particles in thin foils. The possibility of thin foils being missed by the simulation's tracker was investigated and ruled out.

In the worst case scenario where the extra material is at the surface of the production target, the systematic uncertainty due to multiple scattering in the target (see Section 9.5) increases by  $0.7 \times 10^{-4}$ , which is negligible. Since the true cause of the discrepancy is probably within the detector itself, where it does not cause a problem for  $P_{\mu}^{\pi} \xi$ , no systematic uncertainty is assigned due to muon ranging.

---

<sup>25</sup>The muon scintillator was not properly weighed before construction, and was assumed to be 8 thou instead of its correct thickness of 10 thou.

Table 3.1: Materials seen by a muon reaching the centre of an aluminium target. The range of surface muons ( $p = 29.79 \text{ MeV}/c$ ) is  $143 \text{ mg}/\text{cm}^2$  of carbon. Based on Table 2.1 from Ref. [36].

Description	Thickness ( $\text{mg}/\text{cm}^2$ )
Graphite production target	3.5 <sup>a</sup>
Polyester window valve	0.4
Upstream gas degrader foil ("vacuum window")	12.9
Downstream gas degrader foil	0.9
Adjustable degrader gas <sup>b</sup> (He/CO <sub>2</sub> )	3.6 (pure He) to 40.3 (pure CO <sub>2</sub> )
Air	5.2
Muon scintillator	24.8
Scintillator wrapping (Aluminised Mylar)	8.9
Cradle window	0.9
Detector gas (He/N mixture)	12.6
PC module (4 chambers)	9.2
Dense stack (8 chambers)	13.4
Sparse stack (7 chambers)	27.9
Target PCs	4.2
$\frac{1}{2}$ of Al target	9.6
	138.0 to 174.7

<sup>a</sup> This is the average amount of material seen. The momentum resolution of the channel allows muons with a range of production target depths to be accepted.

<sup>b</sup> The gas densities in this table assumed an atmospheric pressure of 750 torr, temperature  $31.0^\circ\text{C}$ .

### 3.10 The upstream beam package

The muons encounter a very thin  $3\ \mu\text{m}$  polyester window inside the M13 beam line, at the F1 position, which is designed to stop protons and radioactive ions. The first material seen *after* the beam line is shown in Fig. 3.20, where the muons encounter a vacuum window at the end of the beam line. The other components in the figure make up a removable upstream beam package. This first encounter does not take place until the muons are inside the yoke, and the field is already at 70% of its maximum.

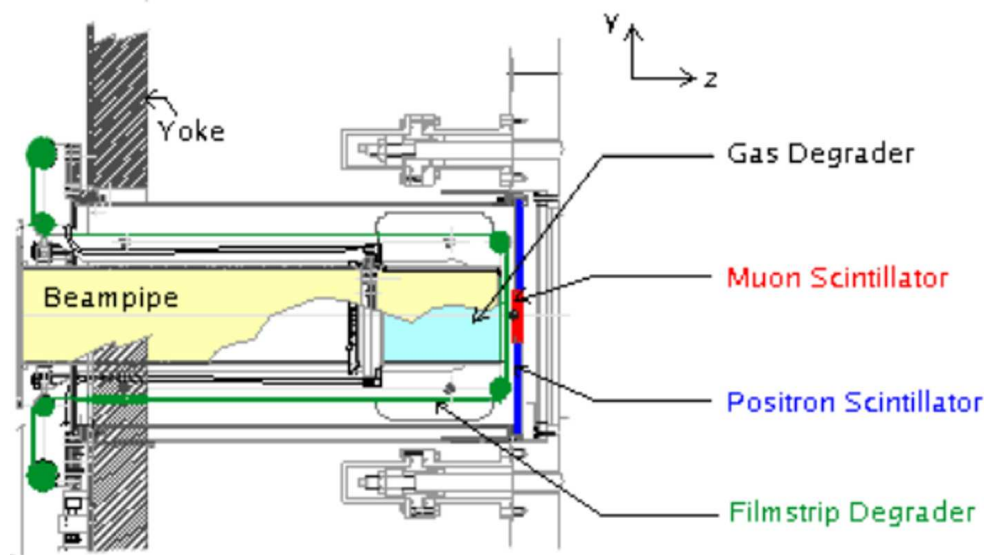


Figure 3.20: Beam package for upstream end of detector. Note the beam does not encounter material until the upstream window the gas degrader. This figure was originally Fig. 2.12 in Ref. [36].

Figure 3.20 shows a gas degrader of length 20.4 cm, which was filled with a helium / carbon dioxide mixture. The gas ratio was automatically adjusted to stabilise the muon stopping distribution, in response to ambient pressure changes. In the previous  $P_{\mu}^{\pi} \xi$  analysis the feedback loop was only in operation towards the end of data acquisition. The original design specification estimated the helium and carbon dioxide should have a 50:50 volume ratio. In the winter of 2006 the degrader typically contained  $\approx 35\%$   $\text{CO}_2$  by volume, and in the summer of 2007 the fraction was  $\approx 43\%$ . For the previous  $P_{\mu}^{\pi} \xi$  analysis the fraction was  $\approx 37\%$ .

Figure 3.20 shows a central muon scintillator, which provided the trigger for the experiment, and an annular positron scintillator, which was used in determining the wire time

offsets. The muon scintillator was a circular plastic scintillator of radius 3 cm, thickness  $195\ \mu\text{m}$ , wrapped in aluminised mylar. The electronics threshold was set high to mostly ignore the beam positrons. The muon scintillator was read out with two light guides (M1 and M2), and the coincidence of M1, M2 and M1+M2 was used as the trigger<sup>26</sup>.

The annular scintillator was expected to establish the decay positron track time. However, the helix reconstruction software was able to establish this time itself. Therefore the only use of the annular scintillator was in the calibration of the wire time offsets, which are described in Section 3.15. The scintillator also shielded the upstream half of the detector from backscatters.

Lastly, Fig. 3.20 shows a “filmstrip degrader”. This allowed up to 0.10 cm of Mylar to be put in the path of particles. For nominal data acquisition, this degrader was set to the hole (no material) position. Special data was taken with the muons stopped far upstream in the detector (see Section 6.8), and this required the use of the filmstrip degrader.

This section has described a beam package that is placed *upstream* of the detector stack. In nominal running there is *no* corresponding downstream package, and this is expected to cause an asymmetry in backscatters<sup>27</sup>. In order to study this asymmetry, a copy of the beam package was specially constructed and placed downstream of the detector stack for a single data set.

### 3.11 Muon stopping target

Muons were stopped in high purity foils of silver (2006) and aluminium (2007), which both had purity  $> 99.999\%$ . The aluminium target is the same foil used for the previous  $P_\mu^\pi \xi$  measurement. The thicknesses were  $29.5\ \mu\text{m}$  ( $31\ \text{mg}/\text{cm}^2$ ) for silver, and  $71.0\ \mu\text{m}$  ( $19\ \text{mg}/\text{cm}^2$ ) for aluminium. Both targets were expected to depolarise the muons by a small amount, with a simple exponential form for  $P_\mu(t)$ , as described in Section 2.5.5

The target region is shown in Fig. 3.21, where the metal target is seen to be part of the cathode between PC6 and PC7. The figure shows Kapton masks that avoid problems with high electric fields where the metal target is attached to the aluminised mylar foil.

<sup>26</sup>The coincidence of M1 and M2 is used to suppress false triggers due to photomultiplier noise. The sum of M1 and M2 provides a larger pulse for improved time resolution.

<sup>27</sup>The primary backscatter process in the experiment is a positron rebounding, following a Coulomb interaction with a nucleus. Therefore the number of measured backscatters in the experiment depends on the thickness and positioning of materials outside the tracking volume. Secondary processes such as showering are possible, but for low energy positrons this is less of a problem.

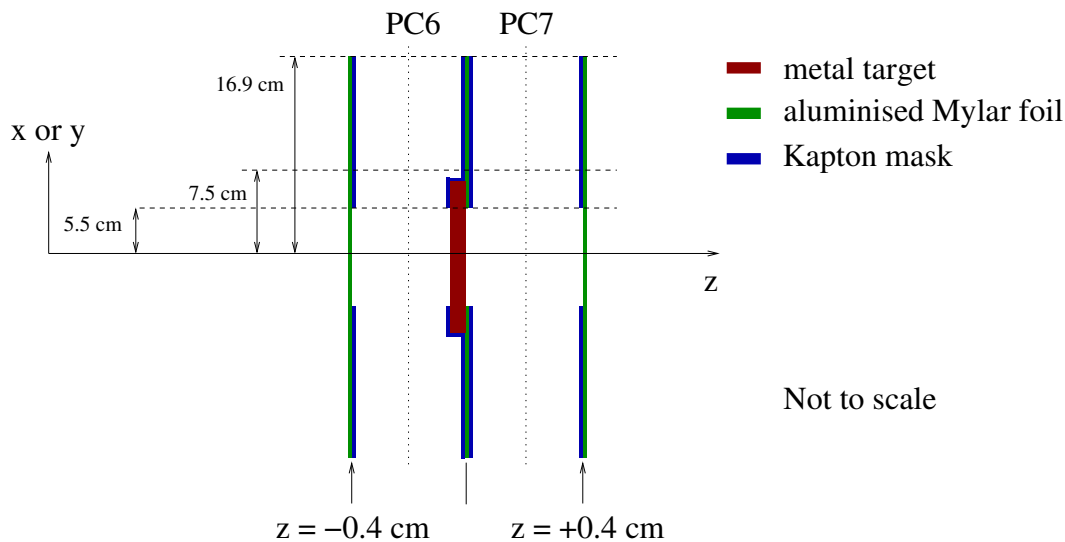


Figure 3.21: Schematic of the muon stopping target, which is part of the cathode foil for PC6 and PC7.

### 3.12 Electronics

The electronics and data acquisition system have been described elsewhere[36, 39, 41]. In summary, time to digital converters (TDCs) record start and stop times for pulses on each wire. The TDCs record everything  $6\ \mu\text{s}$  before the trigger and  $10\ \mu\text{s}$  after the trigger. If the TDCs are busy, or a muon arrives within  $15\ \mu\text{s}$  of the trigger, a new event is *not* started. Instead the hits are recorded and the events are later identified as multiple muons.

An individual TDC can suffer from non-linearities. The internal oscillator may not be exactly at the manufacturer-specified frequency, leading to a so-called “integral non-linearity”. The TDCs used by the experiment (LeCroy model number 1877) had an integral non-linearity of  $< 25\ \text{ppm}$ [43], which is beyond the required accuracy. The TDCs can detect separate edges down to  $20\ \text{ns}$ [44], yet they claim a precision of  $0.5\ \text{ns}$ . The interpolation used to reach the  $0.5\ \text{ns}$  precision introduces a “differentiable non-linearity”. Again, the LeCroy 1877 TDCs had a negligible differential non-linearity of  $\pm 0.1\ \text{ns}$ [43]. The experiment spread signals through multiple TDCs, further reducing the effects of non-linearities. The experiment can measure the correct muon lifetime, confirming that non-linearities are under control.

### 3.13 New downstream trigger

Prior to the measurements in this thesis, there was no reliable downstream trigger available when the experiment's magnetic field was switched on. Therefore in previous analyses the wire timing offsets were only determined at the beginning and end of data acquisition, meaning the measurements were separated by several months. A discrepancy in these measurements contributed a significant systematic in the previous  $P_{\mu}^{\pi} \xi$  result. The author's first project was to help in the design and construction of a reliable downstream trigger to allow continuous monitoring of the timing offsets, even when the magnetic field was at full strength. The final design is photographed in Fig. 3.22, and the scintillators are shown in Fig. 3.23. In summary, two 0.318 cm scintillators separated by 0.318 cm covered the hole in the downstream door of the yoke. The top and bottom of each scintillator were read out by light guides that were matched to long ( $\sim 2$  m) light pipes, which transported the collected light to the photomultiplier tubes located in a relatively weak field region. The four-fold coincidence of these signals was used in the analysis as a reliable downstream trigger.



Figure 3.22: Downstream trigger: photograph of completed frame, lightguides, photomultiplier tubes and scintillators.

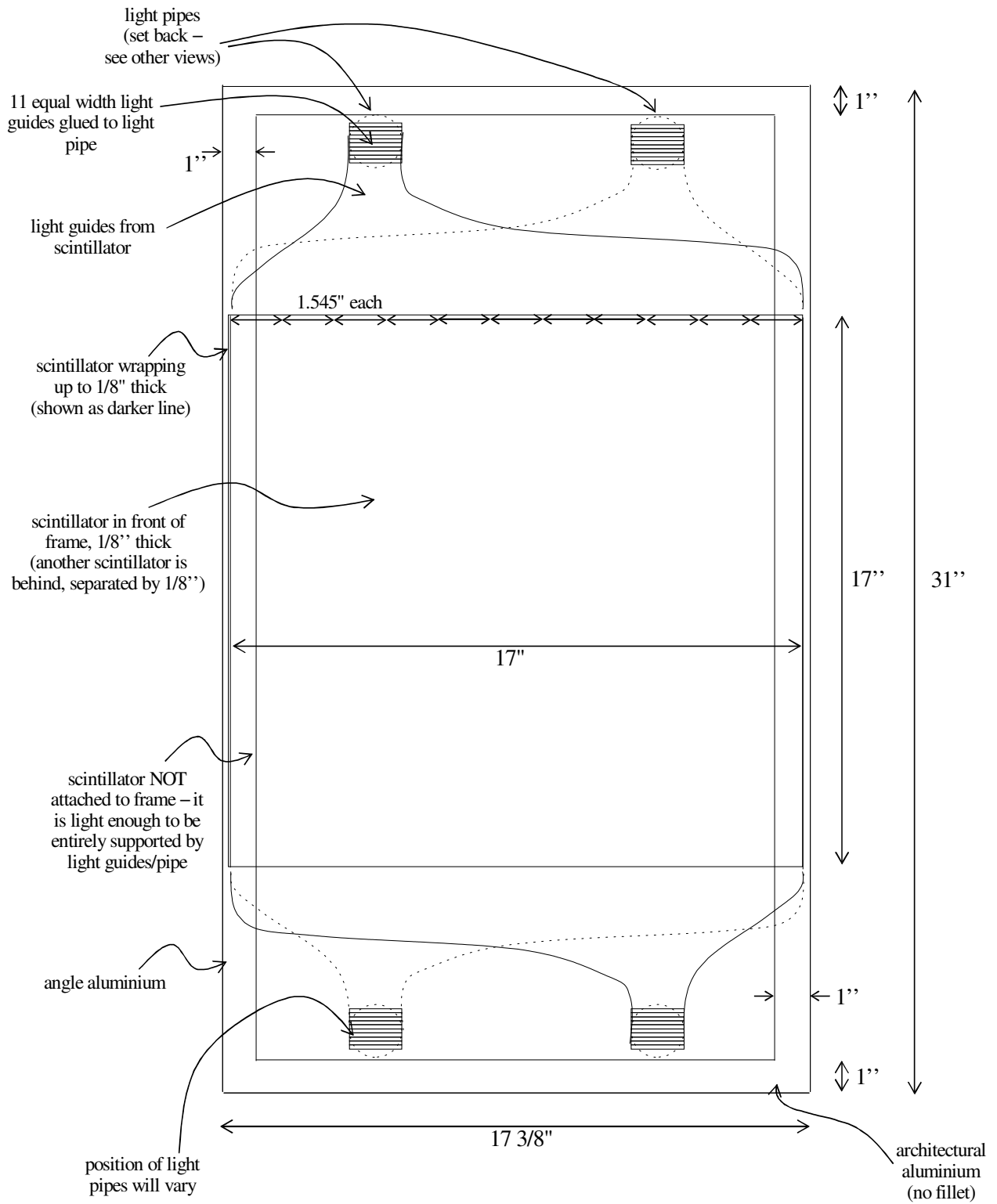


Figure 3.23: Front view (looking downstream) of new downstream trigger.

### 3.14 Alignments

The overall philosophy was to fix the location of the steel yoke, and then align the drift chambers, magnetic field and time expansion chambers to this system. The alignments are shown visually in Fig. 3.24, and summarised in Table 3.2.

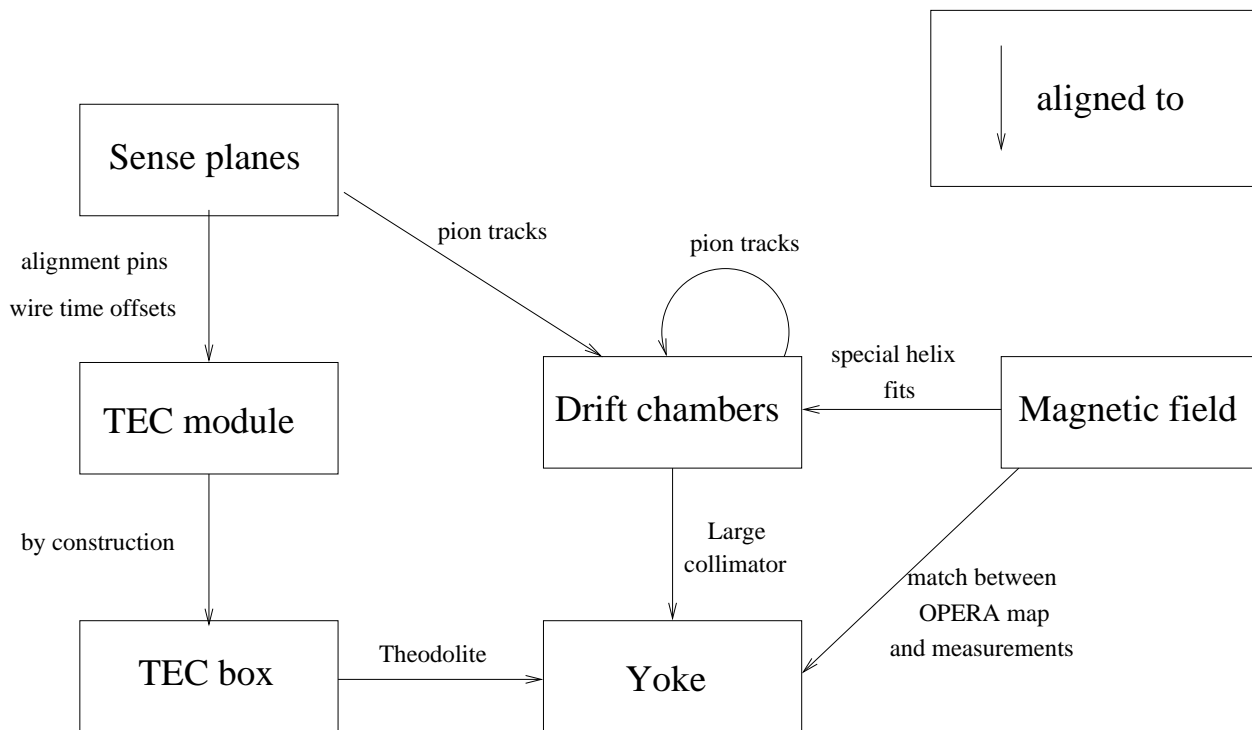


Figure 3.24: Schematic to summarise the relative alignments. The steel yoke is ultimate alignment.

The muon decay spectrum only needs the drift chambers to be aligned to each other in position and angle, and the magnetic field to be aligned relative to the chambers. However the  $P_{\mu}^{\pi} \xi$  measurement must verify the muon beam after the fringe field is matched in data and simulation, requiring the absolute position and angle of the drift chambers to be determined. Additionally the  $P_{\mu}^{\pi} \xi$  measurement requires the beam before the fringe field to be known precisely in position and angle, requiring careful alignment of the TECs.

The sense planes in each TEC module were placed using alignment pins, allowing a precision of  $200 \mu\text{m}$ . The position of each TEC module inside their box was limited by construction. The alignment of the box relative to the yoke was performed using a theodolite. The angle of the sense plane relative to the box containing the TECs was absorbed into the calibration of the wire time offsets. The angle of the sense planes relative to the drift

chambers was determined by turning off the magnetic field, tuning the M13 beam line to accept 120 MeV/c pions, and selecting trajectories that passed through both TEC modules and the detector. These trajectories are well approximated by straight lines, allowing the angle of the sense planes relative to the detector to be determined to better than 1 mr.

The alignment of the drift chambers to the yoke was a new technique for the current analysis. Identical collimators with 14 holes of 2 cm diameter were placed over the upstream and downstream yoke windows. Pions with momentum 120 MeV/c were put through the collimators while the magnetic field was off, and their straight line trajectories were reconstructed with the drift chambers. The drift chambers were consistent with being at  $(x, y) = (0, 0)$ , to a precision of 400  $\mu\text{m}$ . The angle of the stack relative to the yoke was found to be  $-1.4$  mr in  $\theta_x$ , and  $-0.4$  mr in  $\theta_y$ , with a precision 0.1 mr.

The drift chambers were aligned relative to each other using using 120 MeV/c straight line pion trajectories. The drift chamber residuals were minimised to simultaneously determine the translational and rotational alignment. The  $z$  alignment of the chambers is known to a few  $\mu\text{m}$ , as discussed in Section 3.8. Table 3.2 notes the proportional chambers were also aligned, but this was only important for the  $\mu^-$  data, so will not be discussed here.

The magnetic field is rotationally aligned with the drift chambers by applying a special analysis to the nominal muon decay data. Simple helices are fit to the decay positron, with no energy loss or kinks, but the helix is allowed to have a non-zero angle with respect to the chambers. This technique found the magnetic field is misaligned with the drift chambers by 1.15 mr in  $\theta_x$ , and  $-0.33$  mr in  $\theta_y$ .

There are several alignments not under precise control. For example, the translational alignment of the magnetic field (0.2 cm) and the angle of the box containing the TECs.

Long term stability measurements were also taken. For example there were concerns that the box containing the TEC modules may move by small amounts. This could happen when inserting the box and pumping down the beam line to vacuum, and while turning on the 2 T solenoid. There was also the question of reproducibility over a period of several weeks. The position was therefore monitored in three ways: total station<sup>28</sup> measurements at intervals of several months, a laser crosshair directed onto the box while changing the magnetic field, and the same theodolite used for alignment was setup on a catwalk overlooking the beam line. The only conclusive measurement came from the total station, which was accurate to  $\sim 0.1$  cm, and found movements of  $\lesssim 0.1$  cm in  $x$  and  $y$ , but up to 0.4 cm in  $z$ . Fortunately the final polarisation is relatively insensitive to the initial  $z$  position of the beam.

---

<sup>28</sup>A total station measures both position and angle of a target. For this experiment a laser based total station was used. The device could only be used every few months since it was required elsewhere on site, and needed an expert to setup.

Table 3.2: Summary of alignments.

Alignment	Method	Precision	Relative to
Sense planes			
Position	Alignment pins	200 $\mu\text{m}$	TEC module
Angle	Wire time offsets	negligible	TEC module
Angle	Pion tracks	1 mr	DCs
TECs inside box			
Position	Construction	negligible	TEC box
Angle	Construction	3 mr	TEC box
Box containing TECs			
$(x, y)$ position	Theodolite	500 $\mu\text{m}$	Yoke
$z$ position	Total station	0.4 cm	Yoke
Angle	Theodolite	1 mr	Yoke
Drift chambers			
$(x, y)$ position	Large collimator	400 $\mu\text{m}$	Yoke
$z$ position	Ceramic spacers	Few $\mu\text{m}$	Each other
Angle	Large collimator	0.1 mr	Yoke
Position	Pion tracks	< 10 $\mu\text{m}$	Each other
Angle	Pion tracks	< 0.2 mr	Each other
Proportional chambers			
Position	Pion tracks	negligible	Each other
Angle	Pion tracks	negligible	Each other
Magnetic field			
Position	Match of OPERA map to measurements	0.2 cm	Yoke
Angle	Special fits to regular data	0.03 mr	Drift chambers
Angle	Match of OPERA map to measurements	2 mr	Drift chambers

### 3.15 Calibration of wire time offsets

There was a significant effort made to improve the wire time offsets. These are the wire-to-wire differences that come about due to variations in cable lengths (up to  $\sim$  cm), electronics (primarily the TDCs, up to 1 ns), and discriminator amplitude walk. These offsets are used to provide signals to the helix fitting algorithm, which then establishes the track time. Since  $P_\mu^\pi \xi$  is the integrated asymmetry, it is especially sensitive to differences in upstream and downstream track times, making the wire time offsets a crucial calibration. The calibration was carried out for DCs and PCs, but is not important for the PCs since their position resolution is no better than their wire spacing (0.2 cm).

For the previous  $P_\mu^\pi \xi$  measurement, special wire time offset data was taken with the magnetic field off, where pions passed through the entire detector. Low angle straight line pion tracks were selected, and the DC (and PC) signals from the tracks were corrected for time of flight. For each wire the corrected signal time was histogrammed, and then fit to determine the zero-time. Since the magnetic field had to be off, this calibration could only be performed at the beginning and end of data acquisition. In 2004, the calibrations significantly changed over this period, resulting in a large  $P_\mu^\pi \xi$  systematic.

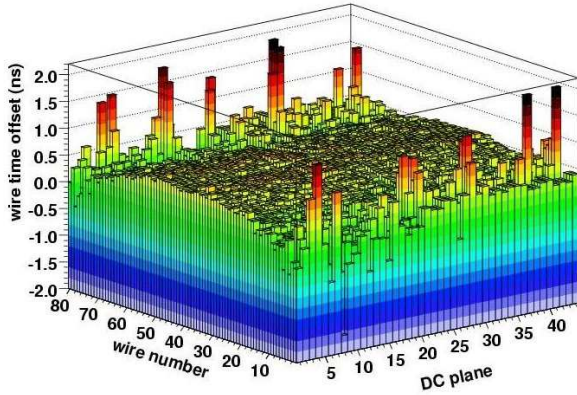
For the current  $P_\mu^\pi \xi$  measurement, the wire time offsets were determined with a new technique that used the nominal decay positrons. A selection was made on positrons that triggered the annular scintillator upstream (see Section 3.10), or the newly constructed downstream scintillator (see Section 3.13). Instead of the straight line fit used for the pions, a simple helix was fit to the decay positrons. This technique had the advantage of significantly improved statistics, and allowed separate wire time offsets to be determined for each data set.

The decay positrons only pass through one half of the detector. The scintillators could be used to relate the upstream and downstream wire time offsets, but these are limited by their timing resolution. Instead an additional analysis selected the beam positrons which passed through the entire detector. These illuminated the central wires and allowed the determination of a very precise relationship between the two detector halves.

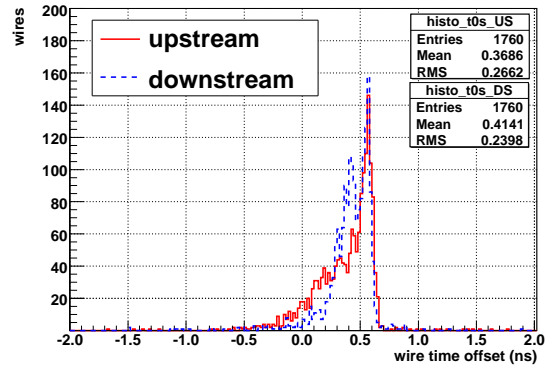
The technique was validated using the simulation, where the wire time offsets are known to be zero. The results are shown in Fig. 3.25(a), where a wire-dependent bias is evident. The wires at the edge of the planes have poor statistics, resulting in anomalous offsets. Figure 3.25(b) shows a histogram of the wire time offsets in each detector half; the bias changes both halves by approximately 0.4 ns. The effect on  $P_\mu^\pi \xi$  of this bias was determined as  $(-0.6 \pm 1.0) \times 10^{-4}$ , which is consistent with zero. Regardless, the simulation used the wire time offsets *after* the calibration technique, so that any bias in the data is included in the

simulation.

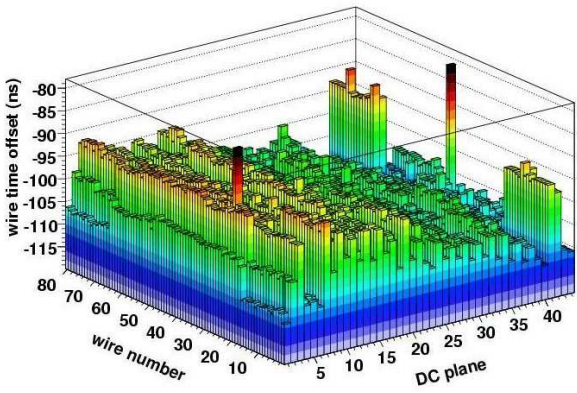
The wire time offsets for one set of the data are shown in Figs. 3.25(c) and 3.25(d). As expected, there is rich structure, and the scale of variations is much greater than the bias shown in Fig. 3.25(a).



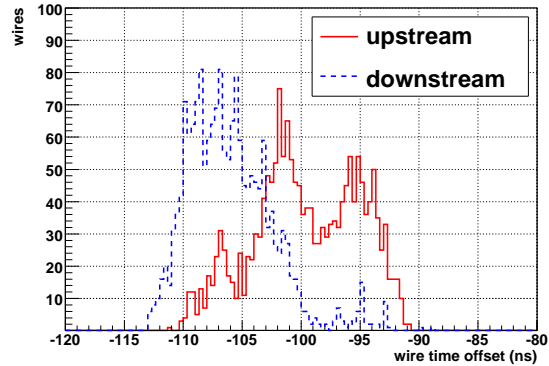
(a) Wire time offset technique applied to simulation. This shows the bias in the technique, since ideally all wires would be at zero.



(b) Simulation wire time offsets.



(c) Wire time offsets for the data. Clearly there is rich structure.



(d) Wire time offsets for the data. Clearly there is rich structure.

Figure 3.25: Wire time offset technique applied to simulation and data.

### 3.16 Calibration of time expansion chambers

The sense planes in the time expansion chambers required the following calibrations: space-time relationship (STR) for each drift cell, wire time offsets for individual wires, global time offset with respect to detector trigger and discriminator amplitude walk. The technique for each will now be summarised.

The STR for each cell was initially generated using the GARFIELD software[45]<sup>29</sup>. The STR for each cell was then corrected using real tracks, since this properly accounts for the interference in electric field between the  $x$  and  $y$  module, as well as voltage and geometry differences from the GARFIELD inputs. Two collimators with 121 holes were placed on each end of the box containing the TECs, as shown in Fig. 3.26(a). This design is an improvement over the published method[30], which described a 49 hole collimator, and the previous  $P_{\mu}^{\pi} \xi$  analysis, which used a four hole collimator[36]. The beam line was tuned to provide a spread muon beam, and low angle tracks were selected. The STRs were adjusted to place the collimator holes at their known positions; Fig. 3.26(b) shows an example of the calibration data after the STRs have been determined.

The relative wire time offsets were determined by selecting tracks from the centre hole of the collimator, and histogramming the times for each wire. The offset required to match the peaks of the histograms was then determined. A global time offset relative to muon scintillator was then determined from the difference in the times between the peak of the wire histograms and the scintillator signal.

The concept of discriminator amplitude walk is shown in Fig. 3.27. The calibration determines the linear relationship between rising edge time and pulse width.

In practice, the relative and global wire time offsets were determined first, followed by the discriminator amplitude walk. The process was then iterated until convergence. The STRs were determined last, also in an iterative procedure.

An engineering run in 2005 found the sense planes became less efficient after several hours of use. For 2006 and 2007 the sense planes were therefore regularly changed. There are other concerns related to the calibration that are reserved for Chapter 5, such as comparisons of the four independent calibrations from 2006/7, the temperature dependence of the STRs, efficiency that depends on distance from the sense plane, and more detailed studies of sense plane aging. The STRs have confirmed to be the same with the magnetic field on and off[30].

---

<sup>29</sup>GARFIELD has been widely used to simulate drift cell response since 1984, and is still actively supported.

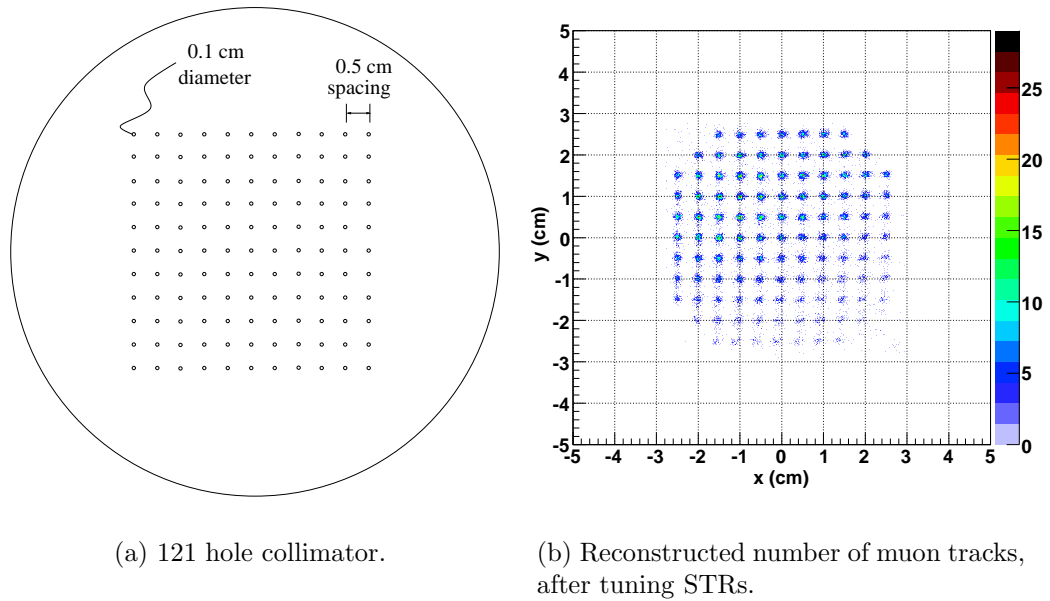


Figure 3.26: Apparatus to determine TEC drift cell space-time relationships (STRs).

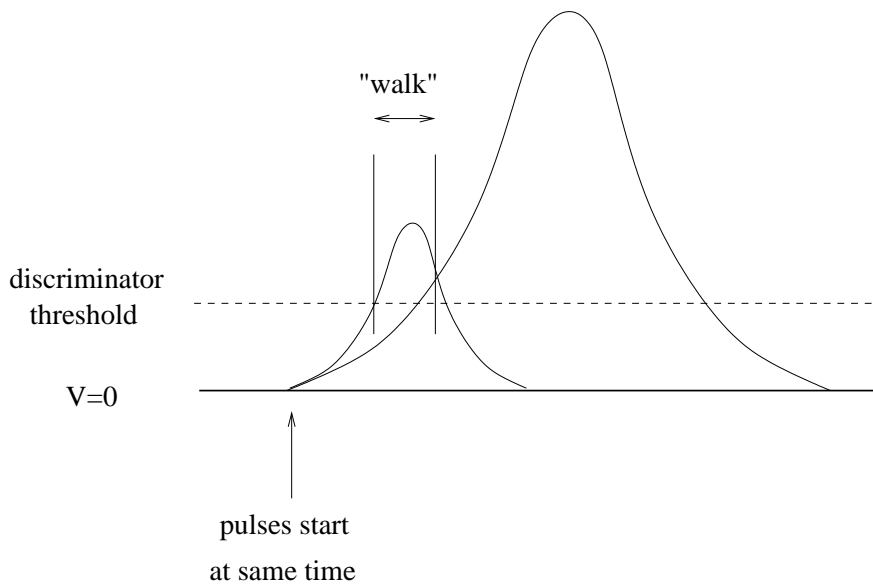


Figure 3.27: Discriminator amplitude walk. Two pulses that start at the same time but have different pulse heights will have different leading edge times.